Available online at www.sciencedirect.com
SCIENCE DIRECT®
Journal of Power Sources 143 (2005) 103–124
JOURNAL OF POWER SOURCES
www.elsevier.com/locate/jpowsour

Three-dimensional model of a complete polymer electrolyte membrane fuel cell – model formulation, validation and parametric studies

Kah Wai Lum[a,*], James Joseph McGuirk[b]

[a] *Institute of High Performance Computing, 1 Science Park Road, #01-01, The Capricorn, Singapore Science Park 2, Singapore 117528, Singapore*
[b] *Department of Aeronautical and Automotive Engineering, Loughborough University, UK*

Received 27 October 2004; accepted 23 November 2004
Available online 18 January 2005

Abstract

A steady-state, three-dimensional model of a complete polymer electrolyte membrane fuel cell (PEMFC), including both the anode and cathode, is formulated and solved using a finite volume computational fluid dynamics (CFD) code, Fuel3D, developed at Loughborough University. The model is first validated against data obtained from the literature on a global basis. It is further validated on a local basis using experimental data obtained from a segmented cell. Excellent agreement is obtained. The validated model is then used to study the effect of electro-osmotic drag and diffusion of water across the membrane. Overall transport of water across the membrane is seen to take place from the anode to the cathode side. Finally, the model has been used to carry out some parametric studies, such as variation of electrode thickness, shoulder width, degree of permeability and oxidant concentration, to provide a clearer understanding on how changes in parameters affect the cell performance.
© 2004 Elsevier B.V. All rights reserved.

Keywords: PEMFC; Mathematical modeling; Water management; Local current density; Parametric studies

1. Introduction

It is known that water content plays a very important role in determining the performance of fuel cells. Too little water will lead to drying of the membrane, which reduces its conductivity. Too much water will cause flooding in the electrodes which hinders the amount of reactant gases from reaching the catalyst sites. In order to understand the transport phenomena that occur, careful modelling of the fuel cell has to be done. Recent one-dimensional models of the PEMFC have been developed by Bernardi et al. [1,2], Springer et al. [3], Eikerling et al. [4], Wöhr et al. [5], Baschuk et al. [6], Rowe et al. [7] and Maggio et al. [8]. These models are useful in providing insight and reasonable predictions of the cell performance in the low and intermediate current density ranges, but fail to reproduce the abrupt drop observed experimentally at high current density. Two-dimensional effects are found to be important and to have a significant impact on some aspects of fuel cell operation and water management in particular. More recent two-dimensional models are given by Nguyen et al. [9,10], Hubertus et al. [11], Scott et al. [12], Squadrito et al. [13], Gurau et al. [14], Yi et al. [15], Singh et al. [16], Dannenberg et al. [17], Hsing et al. [18], Um et al. [19], Paola [20] and Siegel et al. [21].

In order to have a better understanding of how the actual fuel cell performs, it is necessary to have a model which is three-dimensional. This is especially so in the electrode since its role is to allow a spatial distribution of the current density on the membrane in both the direction of bulk flow and the direction orthogonal to the flow but parallel to the membrane. It is also important to include the anode so that the movement of water across the membrane can be accounted for.

Recent three-dimensional works have been published by Shimpalee et al. [22–25], Berning et al. [26–28], Zhou et al. [29], Jen et al. [30], Um et al. [31], Nguyen et al. [32]

* Corresponding author. Tel.: +65 6419 1432.
E-mail address: lumkw@ihpc.a-star.edu.sg (K.W. Lum).

0378-7753/$ – see front matter © 2004 Elsevier B.V. All rights reserved.
doi:10.1016/j.jpowsour.2004.11.032

Nomenclature

a	water activity
A	specific surface area of the control volume (m^{-1})
c_i	concentration of specie i ($mol\,m^{-3}$)
D_{H_2O}	diffusion coefficient of water ($m^2\,s^{-1}$)
$D_{A,B}$	binary diffusion coefficient ($m^2\,s^{-1}$)
F	Faraday constant (96,487 $C\,mol^{-1}$)
I	current density ($A\,m^{-2}$)
I_o	exchange current density ($A\,m^{-2}$)
m_i	mass fraction of species i
M	mixture molar mass ($kg\,mol^{-1}$)
n_d	osmotic-drag coefficient
p	pressure ($N\,m^{-2}$)
P	water saturation pressure ($N\,m^{-2}$)
R	universal gas constant (8.314 $J\,mol^{-1}\,K^{-1}$)
S	source terms ($kg\,m^{-3}\,s^{-1}$)
t_m	membrane thickness (m)
T	temperature (K)
$\boldsymbol{u}$	velocity vector ($m\,s^{-1}$)
V	voltage (V)
V	volume (m^3)
x_i	mole fraction of species i
x	x position coordinate (m)
y	y position coordinate (m)
z	z position coordinate (m)

Greek symbols

α	net water transport coefficient per proton
$\in$	porosity
η	overpotential (V)
κ	permeability (m^2)
μ	viscosity ($kg\,m^{-1}\,s^{-1}$)
ϕ	any variable
ρ	density ($kg\,m^{-3}$)
σ	membrane conductivity (Ω^{-1})

Subscripts and superscripts

a	anode
A	species A
B	mixture B
c	cathode
cr	critical
eff	effective
g	gas
H_2O	water
i	species
K	anode or cathode
m	membrane
np	non-porous
N_2	nitrogen
oc	open circuit
O_2	oxygen
p	porous
sat	saturation

Miscellaneous symbols

$\langle\rangle$	superficial average
$\langle\rangle^g$	intrinsic average

and Senn et al. [33]. These models have only been validated with experimental data from global polarization curves and as such are not validated on a local level, i.e. how well they predict the local current density distribution. In fact, most of the models found in the literature are shown to predict the global fuel cell performance rather well, be it for one- [1–8], two- [21] or three-dimensional [22,23] models. This agreement, irrespective of the dimensionality of the model, might be due to running the experiments under conditions that correspond with the model assumptions/simplifications. However, it is also quite likely that the agreement might be due to parameter adaption to experimental data, usually in the form of global polarization curves.

In view of the number of unknown parameters that arise in fuel cell modeling, the approach of global validation of a model is not sufficient. To extend the work on three-dimensional modeling of polymer electrolyte membrane fuel cells, a model for the whole fuel cell is herein presented and validated against local current density obtained experimentally with a segmented cell, equipped with a flow field comprising of parallel flow channels. Such a comparison of model predictions with local experimental current density lends the model a higher credibility.

The model is similar to that of Shimpalee et al. [22–25], in that conservation of mass, momentum and species in the gas phase are considered on the cathode and anode side. A membrane model derived by Springer et al. [34], together with appropriate boundary and constitutive relations close the model. Contrary to Shimpalee et al. [22–25], however, only the minimum number of species equations are solved, thus reducing the computational cost. Furthermore, the porous nature of the electrodes is treated with proper volume averaged quantities and care is given to proper coupling of these with the free flow in the flow channels.

After a short introduction to the governing equations, boundary conditions and closure relations, a first global validation of the model implemented in the in-house code, Fuel3D [35] is carried out by comparing a simple fuel cell geometry with computational and experimental results from Shimpalee et al. [22], who used a commercial software, Fluent. Finally, a more complex flow geometry, taking into account local validation with experimental data obtained from a segmented cell [36], is considered. The model will then be used to give an insight into the physical behaviour, the distribution of water vapour and the overall cell performance of the fuel cell. Further parametric studies will follow based

on a simplified geometry, which is typical of a geometrically repeating domain unit away from the end effects in a generic fuel cell.

2. Mathematical formulation

The assumptions used in the 3D model are:

- steady state and laminar flow of gases;
- an isothermal cell due to the high thermal conductivity of the solid materials;
- an ideal gas mixture;
- the catalyst layer is homogeneous;
- presence of water is only in the vapour phase. As such, all reference to water in the following text refers to water vapour, except those in the membrane which is in liquid form.

The governing equations consist of the continuity, momentum and the various species transport equations. For porous regions, superficial and intrinsic properties have to be introduced. Superficial averages are defined as:

$$\langle \phi \rangle \equiv \frac{1}{V} \int_V \phi \, \mathrm{d}V \tag{1}$$

and intrinsic as,

$$\langle \phi \rangle^{(g)} \equiv \frac{1}{V^{(g)}} \int_V \phi \, \mathrm{d}V \tag{2}$$

where V is the total volume of the representative elementary volume (REV) and $V^{(g)}$ is the volume of the free pores in the REV. The two averages are related through,

$$\langle \phi \rangle = \in \langle \phi \rangle^{(g)} \tag{3}$$

where $\in = V^{(g)}/V$ is the porosity. To save on notation in the forthcoming model description, the brackets and g superscript on intrinsic properties are omitted.

In this paper, velocity vectors are treated in the superficial averaged form while the pressure, density and species mass fractions are treated in the intrinsic averaged form. The governing equations are presented in Table 1. The equations represent the case of flow in porous media when $0 < \in < 1$. When $\in = 1$, they represent the case of flow in non-porous media. Four species are considered, namely, hydrogen and water on the anode side, and oxygen, nitrogen and water on the cathode side. The source terms $S_{\mathrm{H_2}}$ and $S_{\mathrm{O_2}}$ refer to the depletion of hydrogen and oxygen at the anode and cathode control volumes next to the membrane respectively. $S_{\mathrm{H_2O_a}}$ and $S_{\mathrm{H_2O_c}}$ take into consideration the production of water at the cathode catalyst layer and the transportation of water across the membrane.

Since there are two species on the anode side and three on the cathode side, it is only necessary to solve one species transport equation on the anode side and two on the cathode side. Here, the water transport equation is solved on the anode side while both the oxygen and water transport equations are solved on the cathode side. The water transport equation is chosen on the anode side because it gives a direct coupling of the presence of water between the anode and cathode sides. The other species can be obtained from the constraint that mass fractions must sum to unity. Hence,

$$m_{\mathrm{H_2}} = 1 - m_{\mathrm{H_2O_a}} \quad \text{on the anode side} \tag{4}$$

$$m_{\mathrm{N_2}} = 1 - m_{\mathrm{O_2}} - m_{\mathrm{H_2O_c}} \quad \text{on the cathode side} \tag{5}$$

The following empirical equations are used to calculate various terms in the electrochemical model. These equations are based on the assumption of a hydrated Nafion 117 membrane and are taken directly from the work of Springer et al. [34]. The net water transport coefficient, α, is given by,

$$\alpha(x, y) = n_{\mathrm{d}}(x, y) - \frac{F D_{\mathrm{H_2O}}(x, y)[c_{\mathrm{H_2O_c}}(x, y) - c_{\mathrm{H_2O_a}}(x, y)]}{I(x, y) t_{\mathrm{m}}} \tag{6}$$

Table 1
Governing equations

Governing equations	Mathematical expressions	Source terms
Conservation of mass	$\nabla \cdot \rho \langle \boldsymbol{u} \rangle = S_{\mathrm{ca}}$ or S_{cc}	$S_{\mathrm{ca}} = S_{\mathrm{H_2}} + S_{\mathrm{H_2O_a}}$ at anode/membrane interface $S_{\mathrm{cc}} = S_{\mathrm{O_2}} + S_{\mathrm{H_2O_c}}$ at cathode/membrane interface $S_{\mathrm{ca}} = S_{\mathrm{cc}} = 0$ otherwise
Momentum equations	$\frac{1}{\in^2} \nabla \cdot \rho \langle \boldsymbol{u} \rangle \langle \boldsymbol{u} \rangle = -\nabla p + \frac{1}{\in} \nabla \mu \nabla \langle \boldsymbol{u} \rangle + S_{\mathrm{m}}$	$S_{\mathrm{m}} = -\frac{\mu \langle \boldsymbol{u} \rangle}{\kappa}$ in porous region $S_{\mathrm{m}} = 0$ otherwise
Hydrogen transport equation	$\nabla \cdot \rho \langle \boldsymbol{u} \rangle m_{\mathrm{H_2}} = \nabla \rho D^{\mathrm{eff}}_{\mathrm{A,B}} \nabla m_{\mathrm{H_2}} + S_{\mathrm{H_2}}$	$S_{\mathrm{H_2}} = -\frac{M_{\mathrm{H_2}} I(x,y) A}{2F}$ at anode/membrane interface $S_{\mathrm{H_2}} = 0$ otherwise
Anode water transport equation	$\nabla \cdot \rho \langle \boldsymbol{u} \rangle m_{\mathrm{H_2O_a}} = \nabla \rho D^{\mathrm{eff}}_{\mathrm{A,B}} \nabla m_{\mathrm{H_2O_a}} + S_{\mathrm{H_2O_a}}$	$S_{\mathrm{H_2O_a}} = -\frac{\alpha(x,y) M_{\mathrm{H_2O}} I(x,y) A}{F}$ at anode/membrane interface $S_{\mathrm{H_2O_a}} = 0$ otherwise
Oxygen transport equation	$\nabla \cdot \rho \langle \boldsymbol{u} \rangle m_{\mathrm{O_2}} = \nabla \rho D^{\mathrm{eff}}_{\mathrm{A,B}} \nabla m_{\mathrm{O_2}} + S_{\mathrm{O_2}}$	$S_{\mathrm{O_2}} = -\frac{M_{\mathrm{O_2}} I(x,y) A}{4F}$ at cathode/membrane interface $S_{\mathrm{O_2}} = 0$ otherwise
Cathode water transport equation	$\nabla \cdot \rho \langle \boldsymbol{u} \rangle m_{\mathrm{H_2O_c}} = \nabla \rho D^{\mathrm{eff}}_{\mathrm{A,B}} \nabla m_{\mathrm{H_2O_c}} + S_{\mathrm{H_2O_c}}$	$S_{\mathrm{H_2O_c}} = \frac{[1+2\alpha(x,y)] M_{\mathrm{H_2O}} I(x,y) A}{2F}$ at cathode/membrane interface $S_{\mathrm{H_2O_c}} = 0$ otherwise

where (x, y) here represents the position on the membrane, $D_{H_2O}(x, y)$ represents the diffusion coefficient of water and $c_{H_2O_a}(x, y)$ and $c_{H_2O_c}(x, y)$ represent the molar concentration of water at the anode and cathode, respectively. *I(x,y)* is the local current density, t_m is the membrane thickness and F is Faraday's constant. The first term on the right hand side, n_d, is the electro-osmotic drag coefficient, describing the amount of water dragged across the membrane by each proton from the anode to the cathode side. The electro-osmotic drag itself is a function of the activity of water on the anode side, a_a, of the MEA (membrane electrode assembly, which consists of the anode electrode, anode catalyst layer, membrane, cathode catalyst layer and cathode electrode). The electro-osmotic drag coefficient is calculated as,

$$n_d(x, y) = 0.0049 + 2.02a_a - 4.53a_a^2 + 4.09a_a^3 \quad \text{if} \quad a_a \leq 1 \tag{7}$$

$$n_d(x, y) = 1.59 + 0.159(a_a - 1) \quad \text{if} \quad a_a > 1 \tag{8}$$

It is observed that at high current density, the amount of water dragged across the membrane from anode to cathode is greater than the back diffusion from cathode to anode (second term on the right in Eq. (6)). This results in a net transport of water from anode to cathode side, resulting in possible dehydration on the anode side. Hence, it is reasonable to assume that the water content in the membrane is more likely to be lower on the anode side than on the cathode side, and consequently the activity of water on the anode side can be used to calculate the electro-osmotic coefficient across the whole membrane. The water diffusion coefficient, D_{H_2O} is calculated from,

$$D_{H_2O}(x, y) = 5.5 \times 10^{-11} n_d \exp^{[2416((1/303)-(1/T))]} \tag{9}$$

The water concentration on the anode and cathode sides, $c_{H_2O_a}$ and $c_{H_2O_c}$ in Eq. (6), can be obtained from,

$$C_{H_2O,K}(x, y) = \frac{\rho_{m,dry}}{M_{m,dry}}(0.043 + 17.8a_K - 39.8a_K^2 + 36.0a_K^3) \quad \text{if} \quad a_K \leq 1 \tag{10}$$

$$C_{H_2O,K}(x, y) = \frac{\rho_{m,dry}}{M_{m,dry}}(14 + 1.4(a_K - 1)) \quad \text{if} \quad a_K > 1 \tag{11}$$

(K = either a or c for anode/cathode side, respectively). $\rho_{m,dry}$ is the dry PEM material density while $M_{m,dry}$ is the equivalent weight of a dry PEM. The activity of water is defined as,

$$a_K(x, y) = \frac{x_{H_2O,K}(x, y)p(x, y)}{P^{sat}_{H_2O,K}} \tag{12}$$

where p is the cell pressure and $x_{H_2O,K}$ is the mole fraction of water on either the anode or cathode side. The saturated vapour pressure of water, which is dependent on the temperature, is estimated from,

$$\begin{aligned} P^{sat}_{H_2O,K} = [&0.00644367 + 0.000213948(T - 273.0) \\ &+ 3.43293 \times 10^{-5}(T - 273.0)^2 - 2.70381 \\ &\times 10^{-7}(T - 273.0)^3 + 8.77696 \times 10^{-9} \\ &\times (T - 273.0)^4 - 3.14035 \times 10^{-13}(T - 273.0)^5 \\ &+ 3.82148 \times 10^{-14}(T - 273.0)^6] \times 1.013 \times 10^5 \end{aligned} \tag{13}$$

Eqs. (6)–(13) allow the source terms in the species transport equations to be calculated (assuming the local current density is known). For binary gas mixtures at low pressure, $D_{A,B}$ is obtained from [37],

$$\frac{pD_{A,B}}{(p_{crA}p_{crB})^{1/3}(T_{crA}T_{crB})^{5/12}((1/M_A) + (1/M_B))^{1/2}} = a\left(\frac{T}{\sqrt{(T_{CrA}T_{crB})}}\right)^b \tag{14}$$

where p_{cr} is the critical pressure and T_{cr} is the critical temperature. T is the cell temperature and M_i is the molar mass of the species considered. The values of a and b are taken to be 3.64×10^{-4} and 2.334, respectively. The effective diffusion coefficient applicable to the porous regions will be given by applying the Bruggeman relationship [38],

$$D^{eff}_{A,B} = \in^{1.5} D_{A,B} \tag{15}$$

The mixture viscosity can be obtained from,

$$\mu = \sum\nolimits_{i=1}^{n} \mu_i m_i \tag{16}$$

where the individual species viscosity, μ_i, can be obtained from gas tables at a given temperature. In this work, the mixture viscosity is assumed to be constant and independent of temperature variation. The mixture density is calculated from the ideal gas law,

$$\rho = \frac{pM}{RT} \tag{17}$$

where R is the gas constant and M is the mixture molar mass which is related to the individual species molar mass by the following equation,

$$\frac{1}{M} = \sum_{i=1}^{n} \frac{m_i}{M_i} \tag{18}$$

The species molar fraction can be determined from,

$$x_i = m_i \frac{M}{M_i} \tag{19}$$

The local current density of the fuel cell is given by the following equation,

$$I(x, y) = \frac{\sigma_m(x, y)}{t_m}[V_{oc} - V_{cell} - \eta(x, y)] \quad (20)$$

where V_{oc} is the open circuit cell potential, V_{cell} is the cell potential and σ_m is the membrane conductivity, which is a function of water content, and is determined from,

$$\sigma_m(x, y) = 100\left[0.00514\left(\frac{M_{m,dry}}{\rho_{m,dry}}\right)c_{H_2O_a}(x, y) - 0.00326\right] \exp^{[1268((1/303)-(1/T))]} \quad (21)$$

The cell overpotential, η, is a function of local current density, the exchange current density at one atmosphere of oxygen, and the partial pressure of oxygen. Only the cathode overpotential is being considered here since the anode overpotential is usually an order of magnitude smaller than that of the cathode, and hence can be neglected. The cell overpotential can be calculated from,

$$\eta(x, y) = \frac{RT}{0.5F}\ln\left[\frac{1.013 \times 10^5 I(x, y)}{I_0 P_{O_2}(x, y)}\right] \quad (22)$$

where I_o is the exchange current density at one atmosphere of oxygen and P_{O_2} is the partial pressure of oxygen on the cathode side.

In the current CFD code, the velocity-pressure solution algorithm used is the steady state semi-implicit method for pressure-linked equations (SIMPLE) algorithm [39]. This algorithm is essentially a guess-and-correct procedure for the calculation of pressure on the co-located grid arrangement. Since the code uses colocated grids, the Rhie and Chow [40] interpolation method is used to avoid the problem of oscillations. A 24 processor Origin 2000 computer is used to run the simulations. The solution is considered to be converged when the relative error in each field is less than 10^{-6}.

3. Global validation

A schematic diagram of a typical fuel cell is shown in Fig. 1 and the geometrically repeating domain unit which can be identified away from the end effects regions is presented in Fig. 2. The computational domain consists of an anode gas channel, an anode electrode, a cathode electrode and a cathode gas channel. The membrane and catalyst layers are so thin compared to the electrodes that they are represented as a boundary between the anode and cathode porous electrodes. The anode/cathode electrode interface is a boundary on which conditions representing the membrane/catalyst layers will be applied. The boundary conditions are given in Appendix A.

No distinction was made between intrinsic and superficial variables in [22]. The porosity was taken to be equal to one and only the diffusion coefficient of each species was reduced by a factor of 0.5 to account for porosity and tortuosity. The same will be applied here, but only to allow direct comparison with [22]. In general, as has been shown in [35], it is important to take proper account of the nature of the volume averaged variables being used.

For this simulation, the grids were fixed at 10 cells in the *i*-direction (x), 10 cells in the *j*-direction (y) and 200 cells in the *k*-direction (z) for the gas channels, while for the electrodes,

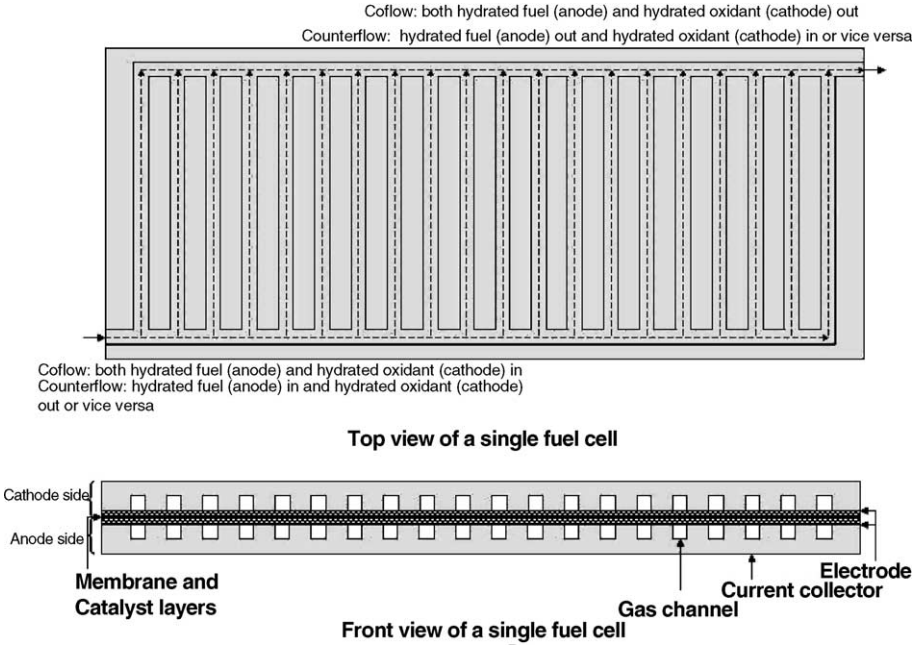

Fig. 1. Schematic diagram of a single fuel cell configuration.

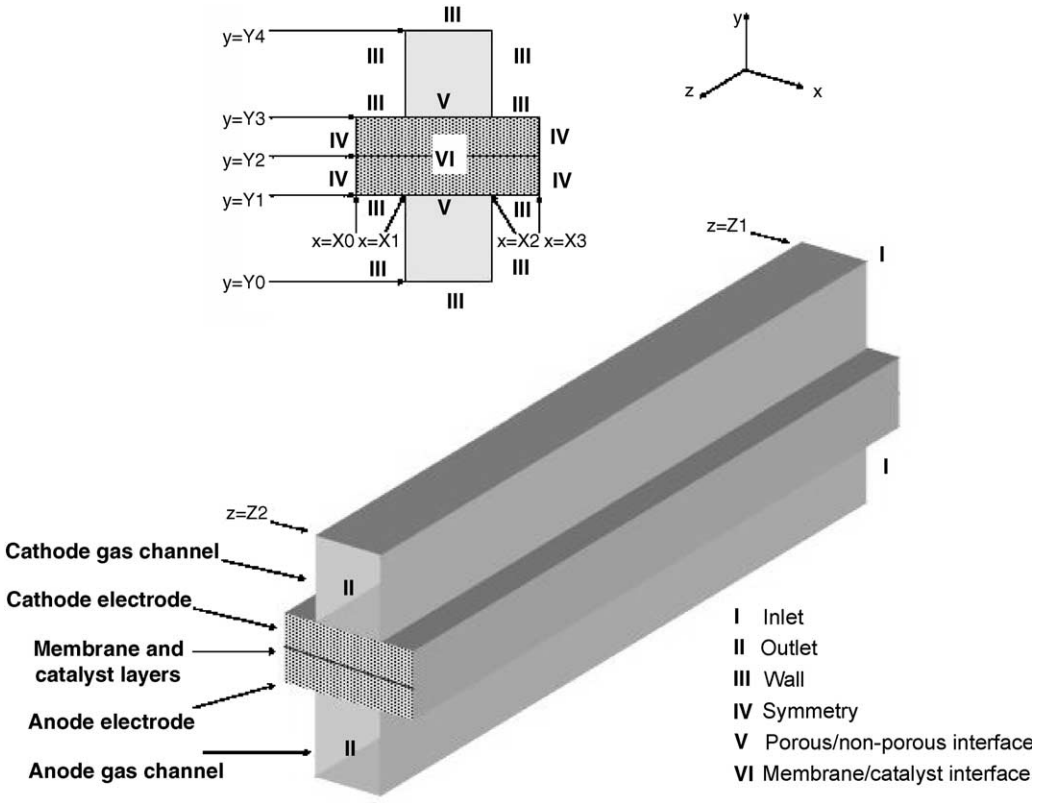

Fig. 2. Schematic diagram for a repeating unit of a complete anode/cathode assembly for a PEMFC.

they were fixed at 38 cells in the *i*-direction (*x*), 10 cells in the *j*-direction (*y*) and 200 cells in the *k*-direction (*z*), after a grid dependence test was carried out.

In order to compare the numerical results with [22], four different cases were considered: very low humidity, low humidity, high humidity and very high humidity (on the cathode side) while all other parameters were kept constant.

Fig. 3 shows the comparison of results between those reported in [22] and the present model. The operating conditions are given in Table 2. All the four cases considered are in coflow. Current density is presented as a ratio because in the work of [22], the experimental data were obtained based on a pressure of 2 atm while numerical predictions were carried out based on an operating pressure of 1 atm. It can be seen

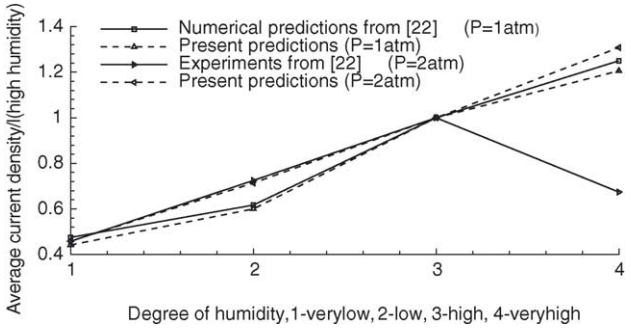

Fig. 3. Average current density ratio dependence on the inlet humidity.

that the results obtained from the present model are in excellent agreement with the numerical ones from [22] for all the cases considered. Good agreement is also obtained with the experimental results obtained in [22], except for the case of very high humidity. As the degree of humidity increases, the average current density increases. This is due to the fact that the amount of current obtained is strongly related to the degree of hydration of the membrane (Eqs. (20) and (21)). As a result, as the humidity increases, the membrane is more hydrated, resulting in better performances. However, this is only true if the electrode is not flooded with excess liquid water which acts as a barrier to the transport of reactant gases to the catalyst layer where electrochemical reaction takes place. This can be seen to occur in the experimental result at very high humidity. Hence, the drop in current density from the experimental data is not observed in the simulated result since in the present model, water is only considered in the vapour phase.

Another point to note is that in [22], five transport equations were solved, namely, hydrogen and water on the anode side, and oxygen, nitrogen and water on the cathode side. However, in the present model, only water on the anode side, and oxygen and water on the cathode side were solved. The remaining species, such as hydrogen on the anode side and nitrogen on the cathode side can be obtained by the mass balance of total species present on each side. This will be more efficient as it reduces the number of equations to be solved numerically, as was also done by [19,26,29].

Table 2
Values of geometry and empirical parameters used in the base case (reported data used in [22])

Channel width	8.0×10^{-4} m
Channel height	1.0×10^{-3} m
Channel length	0.1 m
Electrode width	3.2×10^{-3} m
Electrode height	2.5×10^{-4} m
Electrode length	0.1 m
Membrane thickness (t_m)	5.0×10^{-5} m
Permeability of electrode (κ)	2.0×10^{-10} m^2
Porosity of electrode ($\in$)	1.0
Flow conditions at:	
Very low humidity	
Anode	
Inlet velocity	1.735 m s^{-1}
Mass fraction of H_2	0.727
Mass fraction of H_2O	0.273
Mixture viscosity	1.161×10^{-4} kg m^{-1} s^{-1}
Re	4
Cathode	
Inlet velocity	7.33 m s^{-1}
Mass fraction of O_2	0.225
Mass fraction of N_2	0.751
Mass fraction of H_2O	0.024
Mixture viscosity	2.87×10^{-5} kg m^{-1} s^{-1}
Re	258
Low humidity	
Anode	
Inlet velocity	1.83 ms^{-1}
Mass fraction of H_2	0.635
Mass fraction of H_2O	0.365
Mixture viscosity	1.52×10^{-4}kg m^{-1} s^{-1}
Re	36
Cathode	
Inlet velocity	7.91 m s^{-1}
Mass fraction of O_2	0.225
Mass fraction of N_2	0.734
Mass fraction of H_2O	0.046
Mixture viscosity	3.71×10^{-5} kg m^{-1} s^{-1}
Re	214
High humidity	
Anode	
Inlet velocity	2.21 m s^{-1}
Mass fraction of H_2	0.406
Mass fraction of H_2O	0.594
Mixture viscosity	2.415×10^{-4} kg m^{-1} s^{-1}
Re	3
Cathode	
Inlet velocity	9.05 m s^{-1}
Mass fraction of O_2	0.21
Mass fraction of N_2	0.705
Mass fraction of H_2O	0.085
Mixture viscosity	5.194×10^{-5} kg m^{-1} s^{-1}
Re	176
Very high humidity	
Anode	
Inlet velocity	2.56 m s^{-1}
Mass fraction of H_2	0.295
Mass fraction of H_2O	0.705
Mixture viscosity	2.848×10^{-4} kg m^{-1} s^{-1}
Re	3
Cathode	
Inlet velocity	12.9 m s^{-1}
Mass fraction of O_2	0.187
Mass fraction of N_2	0.61
Mass fraction of H_2O	0.203
Mixture viscosity	9.686×10^{-5} kg m^{-1} s^{-1}
Re	134
Temperature of cell	343 K
Pressure of cell	1.013×10^5 Nm^{-2}
Critical temperature of hydrogen (T_{cr,H_2})	33.3 K
Critical temperature of air ($T_{cr,air}$)	132 K
Critical temperature of oxygen (T_{cr,O_2})	154.4 K
Critical temperature of water (T_{cr,H_2O})	647.3 K
Critical pressure of hydrogen (P_{cr,H_2})	12.8 atm
Critical pressure of air ($P_{cr,air}$)	36.4 atm
Critical pressure of oxygen (P_{cr,O_2})	49.7 atm
Critical pressure of water (P_{cr,H_2O})	221.2 atm
I_o	100.0 A m^{-2}
Dry equivalent weight of PEM ($M_{m,dry}$)	l.l kg mol^{-1}
Open circuit potential	1.1 V
Cell voltage	0.53 V

4. Local validation

Comparison of the predictions for the present model with data obtained from the literature is only a partial validation since only global data (e.g. average current density) could be checked against experimental measurements. This is insufficient as it does not give enough evidence that whatever predicted in the modeled fuel cell is locally correct. Here, validation of the present model against experiment data obtained using a segmented cell (to allow local measurements along the channel) will be carried out. The segmented cell consists of shoulder widths that allow data such as the current density to be measured locally at points along the shoulders. Details of the experimental setup can be found in the work of Potter [36].

The experiments carried out used hydrated hydrogen on the anode side and hydrated air on the cathode side. Experimental data were obtained for different cases by varying the inlet relative humidity and stoichiometry on the cathode side (i.e. relative humidity of 47% at stoichiometry 7, relative humidity of 65% at stoichiometry 3, relative humidity of 83% at stoichiometry 2, in both coflow and counterflow configurations) while keeping all other parameters constant. The base case conditions used for the experiments are summarised in Table 3 [36].

A cross-sectional schematic diagram of part of the complete fuel cell is shown in Fig. 4. The repeating unit identified is given in Fig. 5. This repeating unit will be the solution domain applied for the present model. For the current prediction, the following grid density was applied, after a grid dependence test was carried out: 5 cells in the *i*-direction (*x*), 10 cells in the *j*-direction (*y*) and 200 cells in the *k*-direction (*z*) for the half size gas channels; 10 cells in the *i*-direction (*x*), 10 cells in the *j*-direction (*y*) and 200 cells in the *k*-direction (*z*) for the full size gas channels; and 49 cells in the *i*-direction (*x*),

Table 3
Parameters for local validation of model

Channel width	1.0×10^{-3} m
Channel height	1.0×10^{-3} m
Channel length	0.137 m
Electrode width	6.0×10^{-3} m
Electrode height	2.2×10^{-4} m
Electrode length	0.137 m
Membrane thickness (t_m)	6.0×10^{-5} m
Permeability of electrode (κ)	1.0×10^{-10} m^2
Porosity of electrode (ϵ)	0.4
Anode flowrate	6.84 m/s
Anode mixture density	0.377 kg/m^3
Anode mixture viscosity	2.106×10^{-4} kg m^{-1} s^{-1}
Re_a	12
Case 1	
Cathode stoichiometry ($Re_c = 340$)	7
$\%RH_{anode}$	129
$\%RH_{cathode}$	47
Cathode mixture density	2.989 kg m^{-3}
Cathode mixture viscosity	6.24×10^{-5} g m^{-1} s^{-1}
Cell voltage	0.5 V
Total current	4.15 A
Case 2	
Cathode stoichiometry ($Re_c = 253$)	3
$\%RH_{anode}$	129
$\%RH_{cathode}$	65
Cathode mixture density	3.115 kg m^{-3}
Cathode mixture viscosity	3.16×10^{-5} kg m^{-1} s^{-1}
Cell voltage	0.5 V
Total current	3.5 A
Case 3	
Cathode stoichiometry ($Re_c = 132$)	2
$\%RH_{anode}$	129
$\%RH_{cathode}$	83
Cathode mixture density	3.1 kg m^{-3}
Cathode mixture viscosity	3.548×10^{-5} kg m^{-1} s^{-1}
Cell voltage	0.5 V
Total current	3.1 A
Mole fraction ratio of O_2/N_2	0.21/0.79
Temperature	333 K
Pressure	3.039×10^5
P_{sat}	20178.96 N m^{-2}
Critical temperature of hydrogen (T_{cr,H_2})	33.3 K
Critical temperature of air ($T_{cr,air}$)	132 K
Critical temperature of oxygen (T_{cr,O_2})	154.4 K
Critical temperature of water (T_{cr,H_2O})	647.3 K
Critical pressure of hydrogen (P_{cr,H_2})	12.8 atm
Critical pressure of air ($P_{cr,air}$)	36.4 atm
Critical pressure of oxygen (P_{cr,O_2})	49.7 atm
Critical pressure of water (P_{cr,H_2O})	221.2 atm
I_O	100.0 A m^{-2}
Dry density of PEM ($\rho_{m,dry}$)	2000.0 kg m^{-3}
Dry equivalent weight of PEM ($M_{m,dry}$)	1.1 kg mol^{-1}
Open circuit potential	1.1 V

10 cells in the j-direction (y) and 200 cells in the k-direction (z) for the electrodes. The boundary conditions are given in Appendix A.

Experimental data has been taken from [36] for each of the cases to be studied. Since the value of porosity is not known for the electrodes used in the experiments, two values of porosity are presented as comparison. The current density, species mole fractions and water transport coefficients presented in the following figures are obtained at the centre of the cell (i.e. at $x = 3.0 \times 10^{-3}$ m, $y = 1.22 \times 10^{-3}$ m at the cathode).

4.1. Current density and species distribution

Figs. 6 (a and b), 7(a and b) and 8(a and b) show the current distribution along the channel for a cathode inlet relative humidity of 47%, 65% and 83%, respectively, for both the coflow and counterflow configurations, with a porosity of 0.3 and 0.4. It can be seen that a porosity of 0.3 gives a better fit to the experiment data for the cases of 65% and 83% relative humidity at the cathode while it under-estimates the current density for the 47% relative humidity case. This is true for both the coflow and counterflow configurations.

With a porosity of 0.4, the current density obtained for the 47% relative humidity case shows excellent agreement to that obtained from the experiment. However, they are higher for the cases of 65% and 83% relative humidity. This can be explained by looking at the mole fraction of water on both the anode and cathode side. From Fig. 9(a–c), it can be seen that water concentration at the anode is slightly above that for the liquid water saturation value. This means that water is present in the liquid phase. On the cathode, water is present in the liquid phase almost along the whole channel length, except near the inlet where water is present in the vapour phase. It is therefore likely that liquid water is reducing the available pore volume for the gas flow, especially so at the cathode, resulting in a poorer performance for all three cases considered.

It can also be seen that at a higher inlet relative humidity, a higher water concentration in the liquid phase at the cathode is present along the whole channel length. Since in the model, water is only considered in the gas phase, phenomena such as electrode flooding cannot be captured. This will result in a higher current density obtained for the simulated results compared to the experimental data and this effect will be greater as the relative humidity increases. This explains why the simulated results for the two higher humidity cases produced a current density curve which is higher than that obtained from the experiment while the simulated results for the lowest relative humidity case shows good agreement to the experimental data when a porosity of 0.4 is used. Another point to note is that the reduction in porosity for the two higher humidity cases can effectively represent the pore blockage by the presence of liquid water. Hence, a porosity of 0.4 seems to be a better fit to the experimental data for the 47% relative humidity case while a porosity of 0.3 is a better fit for the two higher relative humidity cases.

One explanation for the disagreement near the outlet may be due to the presence of liquid water in the electrodes. Liquid water tends to be present in greater amount near the exit of the channel since water is accumulated down the channel from the product water as a result of the electrochemical

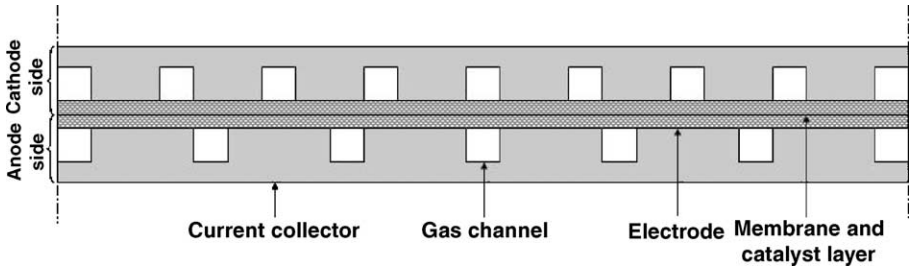

Fig. 4. Cross-section of the cell geometry used in the experiments.

reaction. This can be seen in [41–44] which show that the presence of liquid water does lead to an effective pore blockage. The lower current density obtained in the experiment may be explained by this accumulation of water that caused mass transport limitation of the reactant gases to the catalyst sites for electrochemical reaction to take place. Since in the model, the effect of two-phase flows has not been implemented and all the water produced is assumed to be in the vapour state, which will not result in any pore blockage, such two-phase effects will not be visible. Other reasons for the disagreement could be due to the conditions in which the experiments have been conducted, such as the time the experiment has been allowed to run before data are taken and whether the MEA has been used a couple of times at other operating conditions. All these will affect the experimental data obtained.

Referring back to Fig. 9(a–c), which shows the distribution of species along the channel from the model, it can be seen that due to the high stoichiometry, the mole fractions of oxygen and hydrogen remain virtually constant in the streamwise direction of the cell. The local current density, however, varies significantly (e.g. from 1.2×10^4 A m^{-2} to 8.8×10^3 A m^{-2}). Only the species mole fractions in the coflow configuration for the case of 0.4 porosity is presented for the sake of brevity.

4.2. Cell performance

Returning to the three current density plots (Figs. 6 (a and b), 7(a and b) and 8(a and b)), the case with the highest stoichiometry produced a higher current density along the whole of the channel. This is true for both the coflow and counterflow configurations. The average current densities obtained along the channel for the different cases are given below (at a cell voltage of 0.5 V):

1. At a relative humidity of 47% (stoichiometry = 7), the average current density is 1.0×10^4 A m^{-2} and 1.03×10^4 A m^{-2} for the coflow and counterflow case, respectively.
2. At a relative humidity of 65% (stoichiometry = 3), the average current density is 8.0×10^3 A m^{-2} and

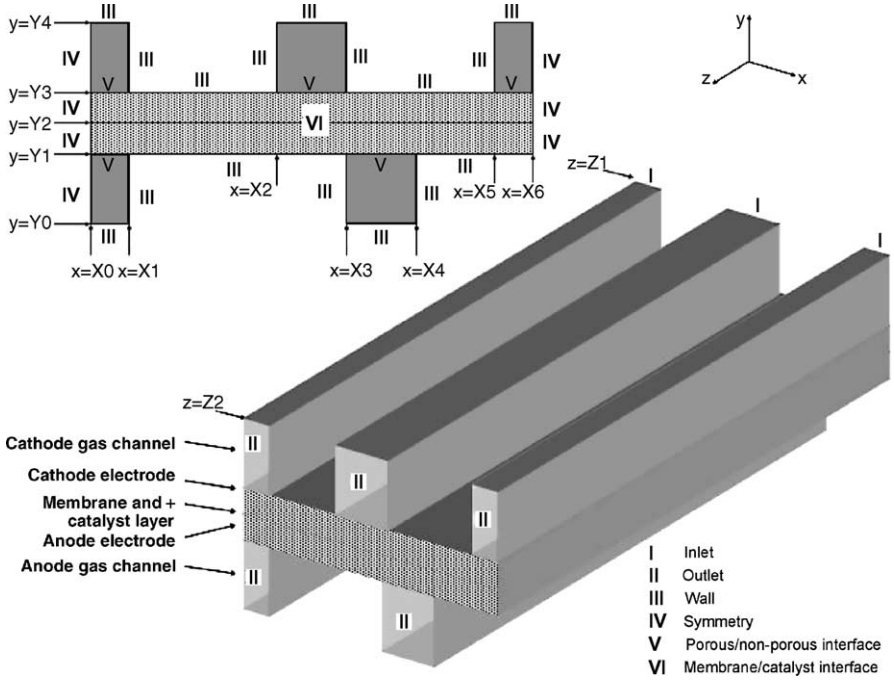

Fig. 5. Repeating unit of the cell used in the experiment and model.

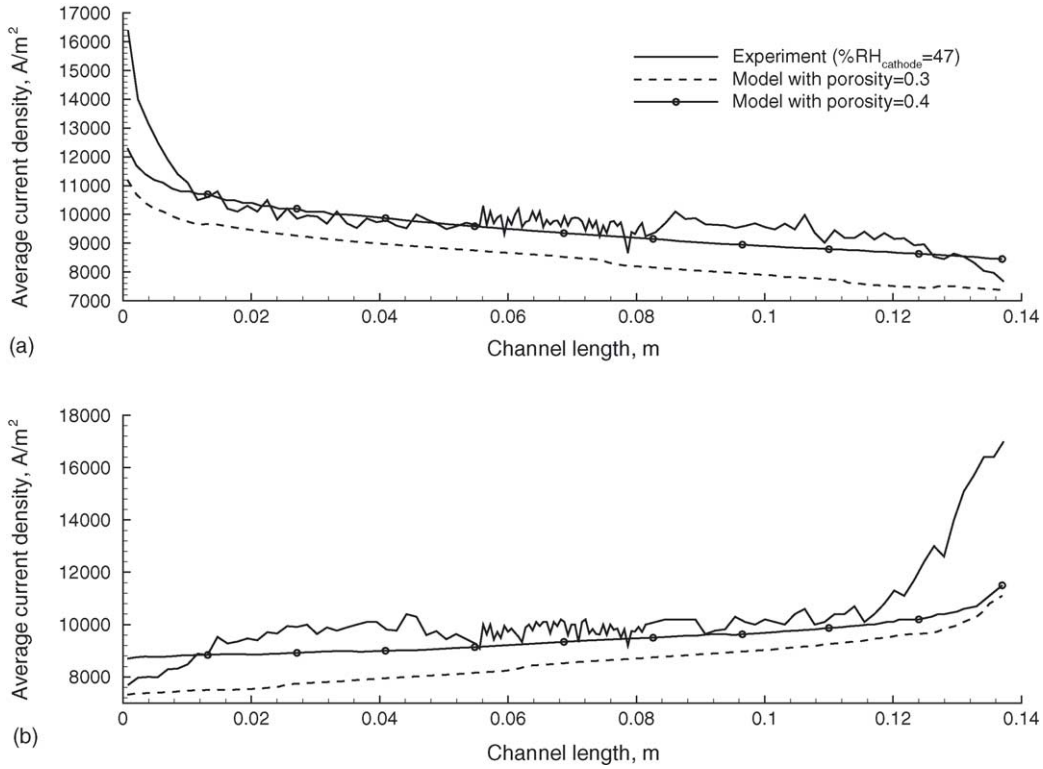

Fig. 6. Local current density down a cathode side gas channel at a cathode relative humidity of 47% in (a) coflow; (b) counterflow.

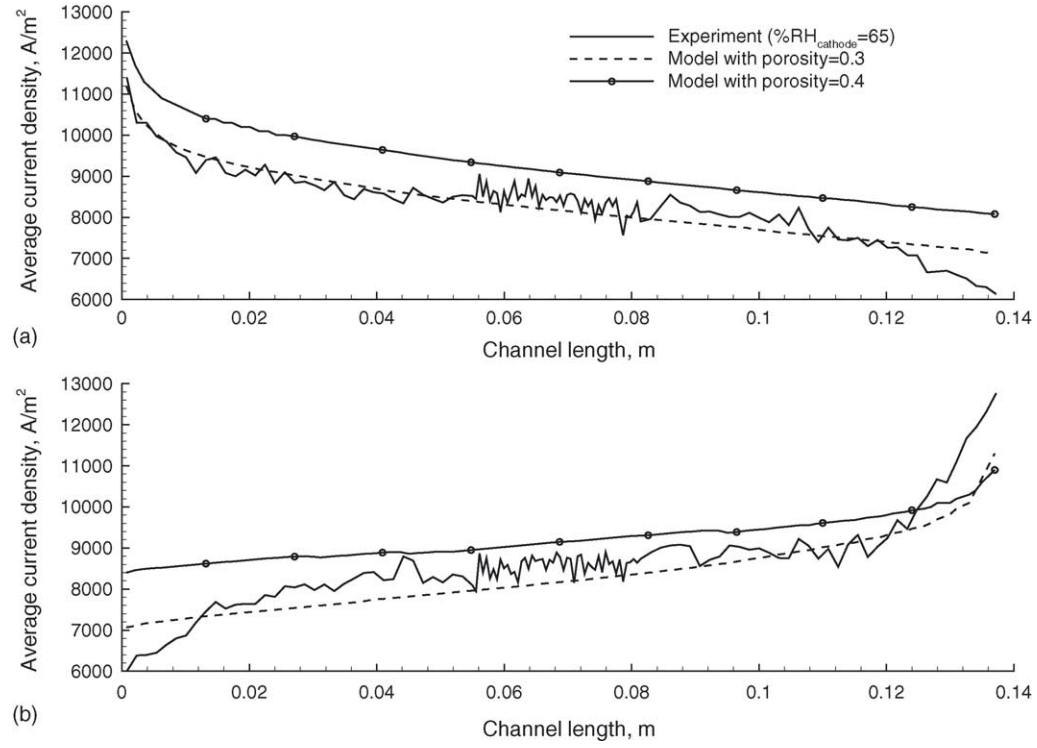

Fig. 7. Local current density down a cathode side gas channel at a cathode relative humidity of 65% in (a) coflow; (b) counterflow.

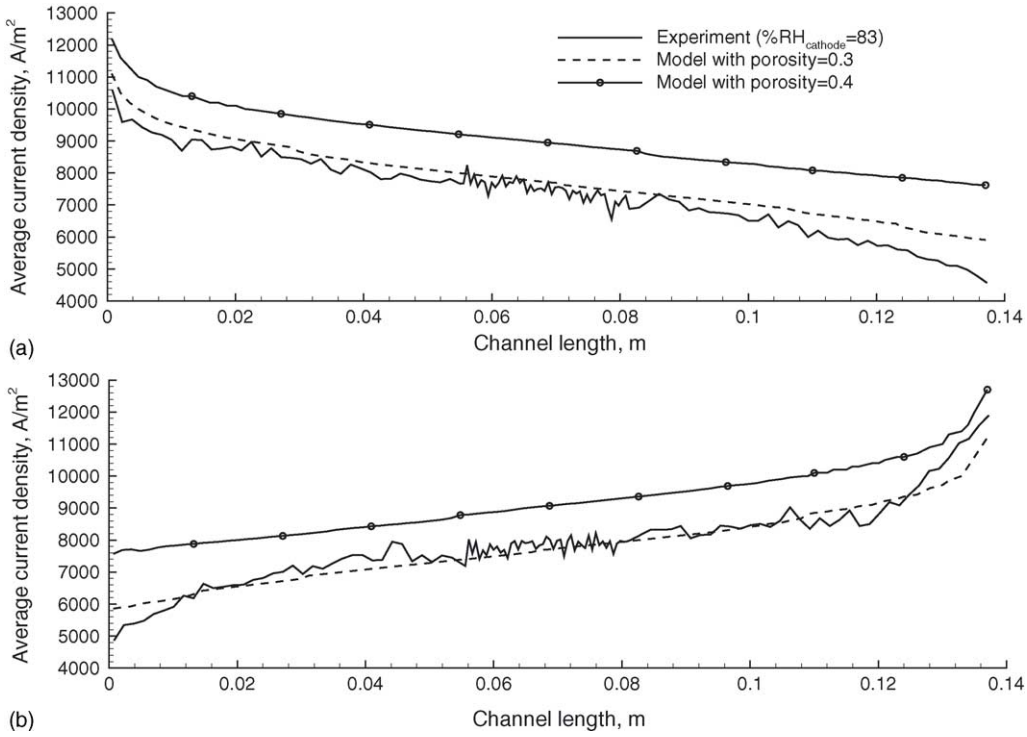

Fig. 8. Local current density down a cathode side gas channel at a cathode relative humidity of 83% in (a) coflow; (b) counterflow.

9.0×10^3 A m^{-2} for the coflow and counterflow case, respectively.

3. At a relative humidity of 83% (stoichiometry = 2), the average current density is 7.0×10^3 A m^{-2} and 8.0×10^3 A m^{-2} for the coflow and counterflow case, respectively.

The reason for this is because a higher inlet velocity will allow a higher concentration of reactant gas to reach the catalyst layer for electrochemical reaction to take place by improved convection. Furthermore, with a lower concentration of water fed into the cell, the degree of mass transport limitation occurring in the electrodes due to pore volume reduction by liquid water will be reduced. In addition, the high velocity helps in removing any excess liquid water from the cell. All these factors work towards a better performance from the fuel cell, provided the amount of water introduced into the cell is still sufficient to keep the membrane well hydrated. Under the present operating conditions, the counterflow configuration tends to produce a marginally higher average current density compared to the coflow configuration.

4.3. Water transport in the membrane

Fig. 10 shows the interaction between the two water transport mechanisms in the membrane of a fuel cell: electro-osmotic drag coefficient and diffusion coefficient at a cathode relative humidity of 47%, 65% and 83%. The net transport of water per molecule of proton across the membrane is also shown. The net transport of water per proton is always a positive number. This means that there is a positive flow of water from the anode to the cathode along the whole channel. In addition, overall diffusion takes place from the cathode to the anode along the whole channel. At the inlet, the amount of reactants and the partial pressure of water are high, leading to high membrane conductivity and hence the local current density is also high. Further down the channel, the membrane becomes dryer due to lower water concentration on the anode side. This causes the membrane conductivity and local current density to decrease. Decreases in local current density then lead to lower water concentration on the cathode side and hence the diffusion coefficient of water from the cathode to anode decreases. The net water transport per proton decreases down the channel since there is less water present down the channel and hence the amount that each proton can drag with it across the membrane decreases.

5. Parametric studies

The following sections will discuss the performance of a PEMFC upon variation in geometrical and operating conditions, based on Fig. 2. To elucidate some of the major contributions/limitations (i.e. cell design and material properties), the following cases were studied: the effect of electrode thickness; the effect of shoulder width with respect to the gas channel width; the permeability effect of the elec-

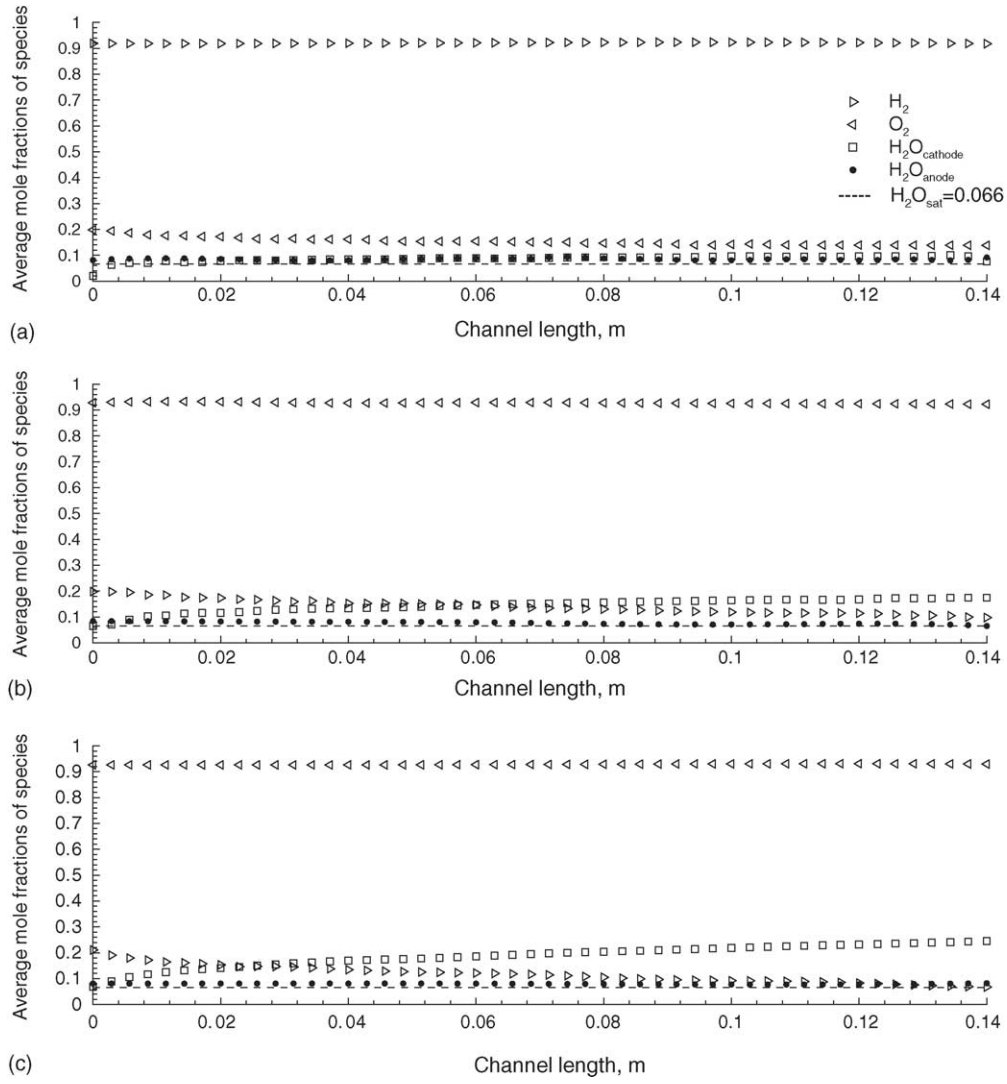

Fig. 9. Local mole fractions of species at cathode relative humidity of (a) 47%; (b) 65%; (c) 83%, in coflow at a porosity of 0.4.

trodes; the effect of using oxygen instead of air. The base case conditions to be used, which are typical for fuel cell operations, are given in Table 4. Otherwise, those from Table 3 are used. Only one parameter was changed from the base case conditions at a time. The boundary conditions are given in Appendix A.

5.1. Parametric variations relevant to cell geometry

In many fuel cell applications, it is important to consider the geometry of the cell so that maximum current can be obtained from as small a cell as possible. This will reduce the cell size, especially in fuel cell stacks, which will make the design more attractive. Hence, considerations have to be made in terms of how many gas channels there should be with respect to the shoulder width in a given area of cell space, and the thickness of the electrodes to be used. These factors will be considered below.

5.1.1. Effect of shoulder width

To study this effect, the gas channel width is kept at 1.0×10^{-3} m while the width of the shoulder is varied between 7.5×10^{-4} m to 2.5×10^{-4} m. The size of the shoulder width affects the performance of the fuel cell in three ways. Firstly, having a smaller shoulder width will enhance the transport of reactant species to the catalyst layer directly above/below the shoulder area. This can be clearly seen in Fig. 11. Fig. 11 shows the distribution of oxygen at the cathode electrode/membrane interface when the shoulder width is varied while keeping the channel width constant. As the shoulder width increases, the oxygen concentration over the shoulder area decreases significantly. This tends to decrease the limiting current density. Furthermore, the oxygen concentration over the channel area is lower since some of the oxygen tends to diffuse to the wider shoulder area.

Secondly, having a smaller shoulder width will increase the contact resistance between the current collector and the

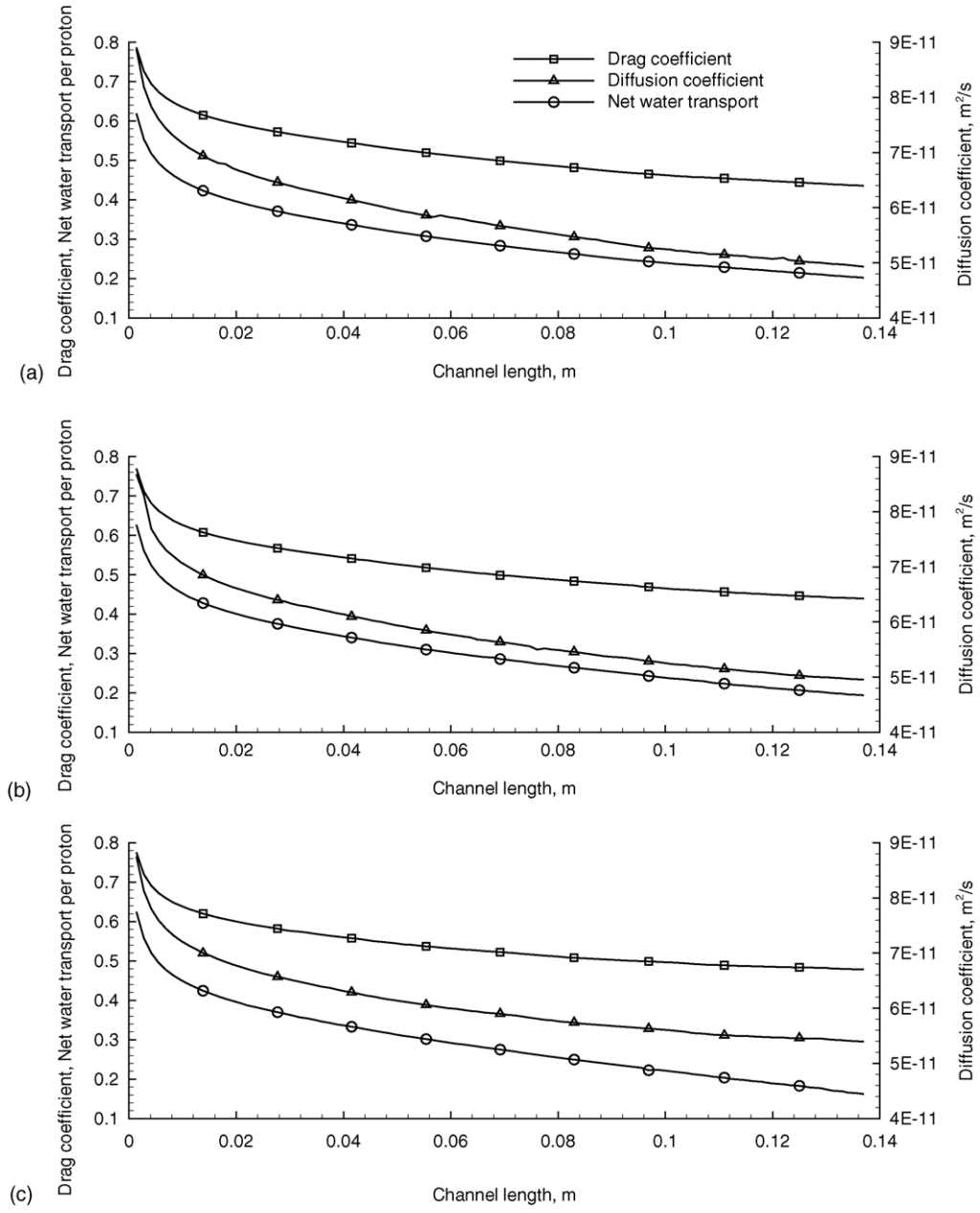

Fig. 10. Electro-osmotic drag coefficient, diffusion coefficient and net water transport across the membrane for a cathode relative humidity of (a) 47%; (b) 65%; (c) 83% in coflow.

MEA. This will lead to greater ohmic loss since there is less contact area to collect the electrons. However, the current density in Fig. 12 shows that as the shoulder width increases, the average current density obtained is lowered (from $1.27 \times 10^4\,\mathrm{A\,m^{-2}}$ to $1.1 \times 10^4\,\mathrm{A\,m^{-2}}$) as a result of the highly reduced oxygen concentration above the shoulder area. Hence, for the present operating conditions, it is advantageous to have a higher oxygen concentration at the cathode electrode/membrane interface by having a smaller shoulder width, provided the properties of the porous backing outlined below are not adversely affected. Thirdly, the ratio between shoulder and channel widths will affect the clamping pressure distribution that the porous backing experiences, which in turn affects properties such as porosity distribution, thermal impedance and contact resistances [45].

The polarization curves shown in Fig. 13(a) show that with a wider shoulder width, mass transport limitation takes place

Table 4
Parameters for parametric studies

Channel length	0.1 m
Electrode width	1.6×10^{-3} m
Electrode height	2.0×10^{-4} m
Porosity of electrode (ϵ)	0.3
$\%RH_{cathode}$	83
Cathode mixture viscosity	$3.36 \times 10^{-5}\,\mathrm{kg\,m^{-1}\,s^{-1}}$
Total current	3.1 A

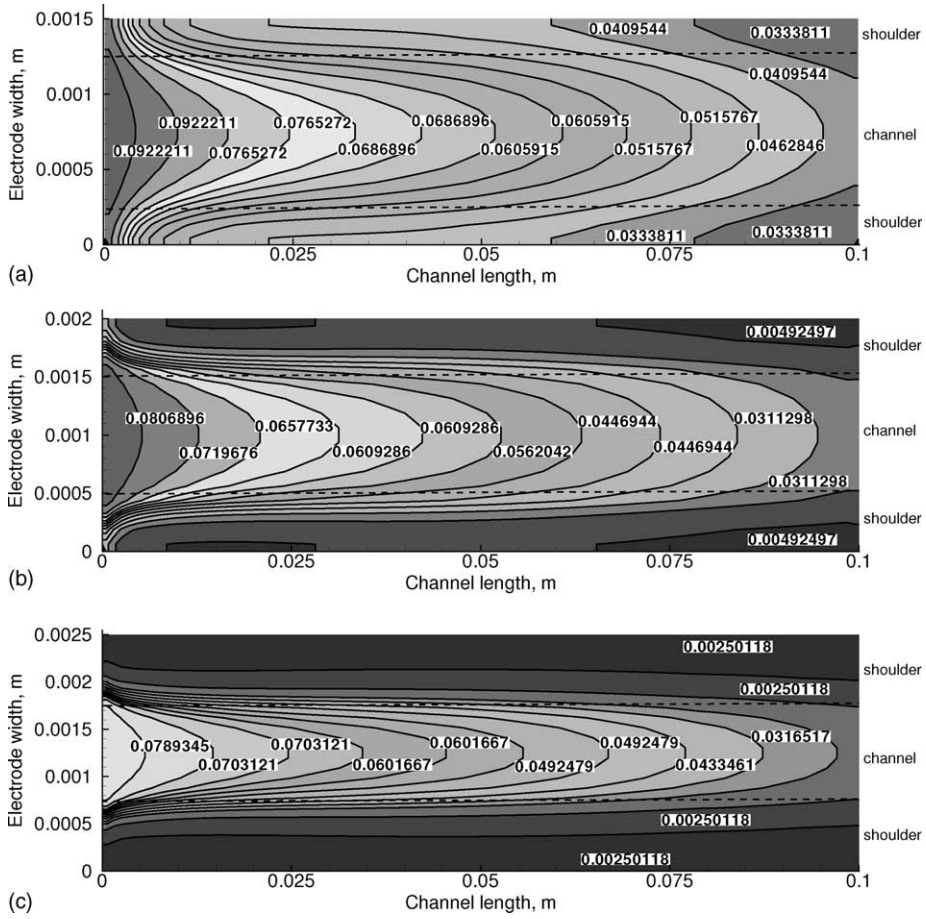

Fig. 11. Mass fraction of oxygen at the electrode/membrane interface with a shoulder width of: (a) 2.5×10^{-4} m; (b) 5.0×10^{-4} m; (c) 7.5×10^{-4} m.

at a lower current density, resulting in a lower maximum peak for the power density curves, Fig. 13(b). Having a ratio of gas channel width to shoulder width of 1.3 (for the case of shoulder width equivalent to 7.5×10^{-4} m) is seen to produce the lowest peak performance. Increasing the ratio to 2 shows an increase in the peak performance. Further increment of the ratio to 4 results in a performance only slightly better than that using a ratio of 2. Hence, optimum gas channel width to shoulder width is seen to occur at a ratio of approximately 2.

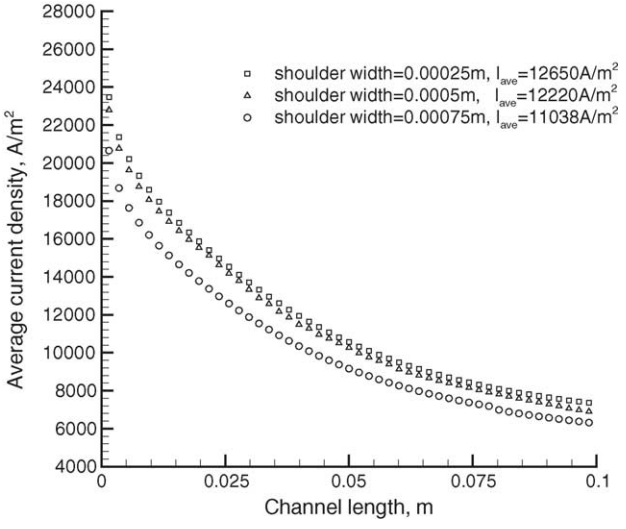

Fig. 12. Average current density at the electrode/membrane interface for the different shoulder widths.

5.1.2. *Effect of electrode thickness*

Four cases of electrode thicknesses are considered, namely: 1.0×10^{-4} m, 2.0×10^{-4} m, 4.0×10^{-4} m and 6.0×10^{-4} m. As the electrode thickness increases, a lower concentration of oxygen is present at the reactive area, as can be seen in Fig. 14. This might easily lead to oxygen depletion at high current density, especially near the end of the channel. However, for a thicker electrode, there is a more even distribution of oxygen concentration between the channel area and the shoulder area since there is more room for diffusion in the spanwise direction.

Fig. 15 shows the average current density obtained down the channel for the different electrode thicknesses. Near the inlet, the thinner electrode produces higher current density. This is because a higher concentration of oxygen reaches the reaction area. However, the thicker electrode outperforms the thinner one 10% down the channel. This is clearly not due to

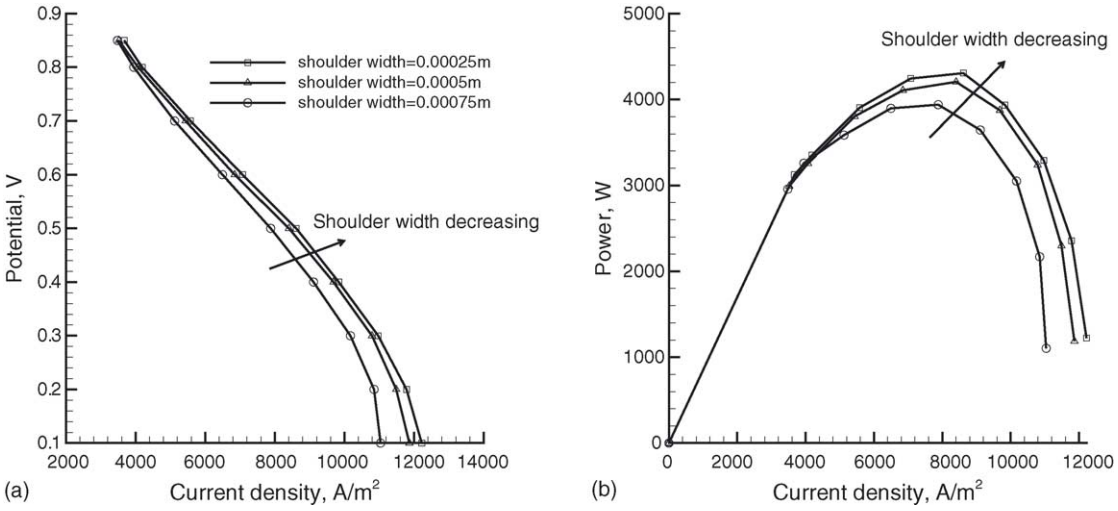

Fig. 13. (a) Polarization curve; (b) power density curve for the various shoulder widths.

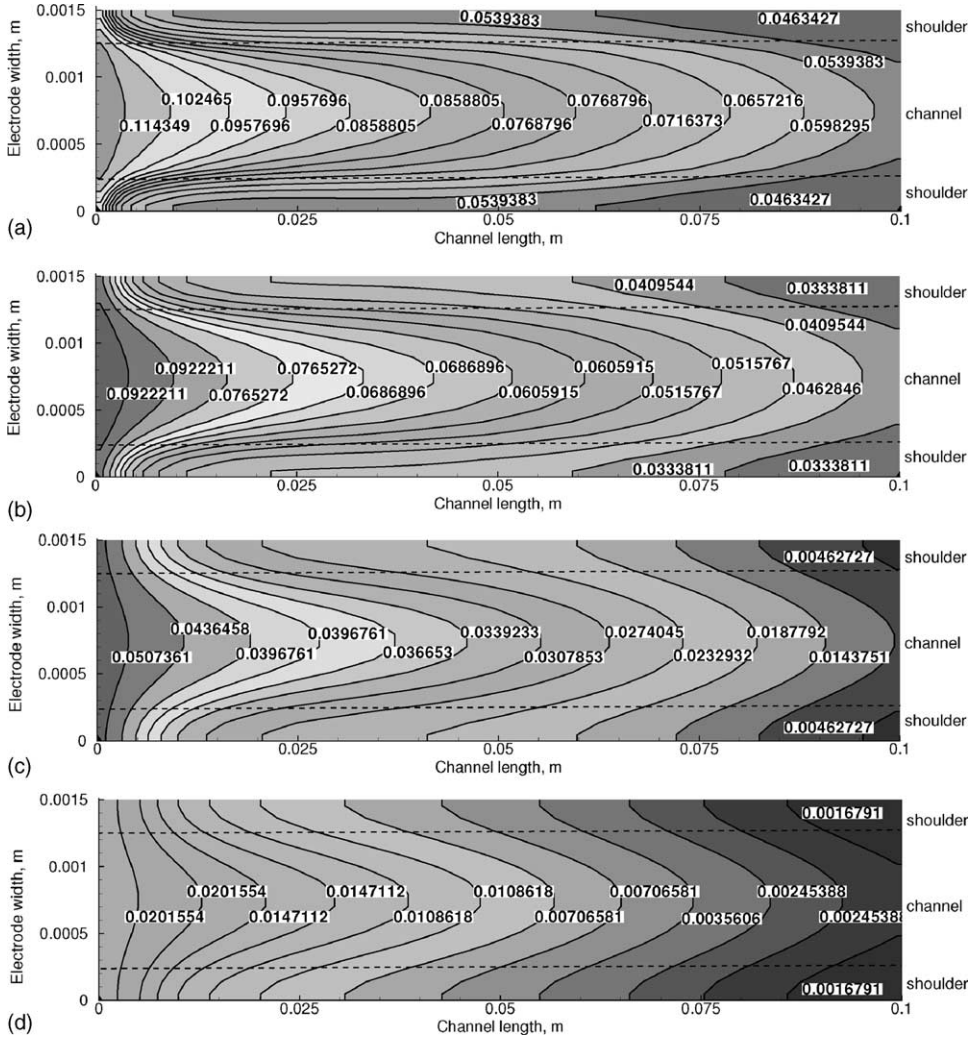

Fig. 14. Oxygen distribution at the cathode electrode/membrane interface at different electrode thicknesses of: (a) 1.0×10^{-4} m; (b) 2.0×10^{-4} m; (c) 4.0×10^{-4} m; (d) 6.0×10^{-4} m.

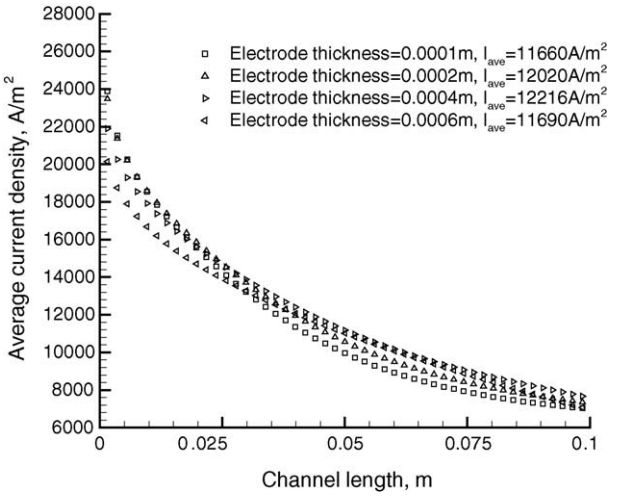

Fig. 15. Average current density at different electrode thicknesses of: (a) 1.0×10^{-4} m; (b) 2.0×10^{-4} m; (c) 4.0×10^{-4} m; (d) 6.0×10^{-4} m.

a reduction in the amount of oxygen in the thinner electrode. The reason may be seen in Fig. 16.

Fig. 16 shows the amount of water present at the anode electrode/membrane interface. As can be seen, about 10% down the channel from the inlet, there is less water available on the thinner electrodes. This results in membrane dehydration and hence reducing the membrane conductivity. As a result, the electrokinetics is limited by the transport of protons across the membrane to the cathode, leading to lower current density. This has happened despite the fact that there is sufficient reactant gas at both the anode and cathode for electrochemical reaction to take place (Figs. 14 and 17). From these results, the importance of keeping the membrane well hydrated to sustain high performance is clearly shown. Increasing the electrode thickness is seen to improve the cell performance to the point where mass transport limitation begins to take place. This occurs for the case where the electrode thickness reaches 6.0×10^{-4} m. There, despite the fact that water is present in higher amounts, hydrogen does

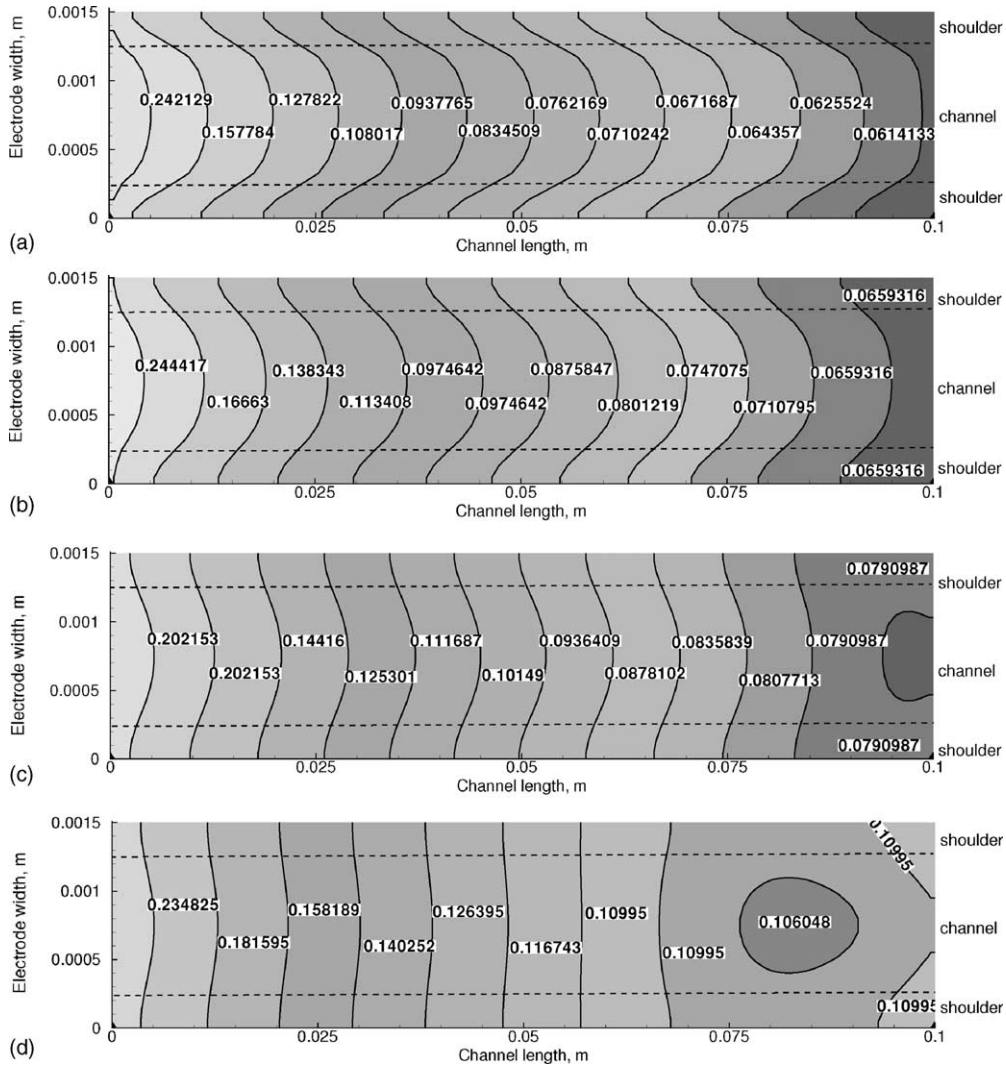

Fig. 16. Water distribution at the anode electrode/membrane interface at different electrode thicknesses of: (a) 1.0×10^{-4} m; (b) 2.0×10^{-4} m; (c) 4.0×10^{-4} m; (d) 6.0×10^{-4} m.

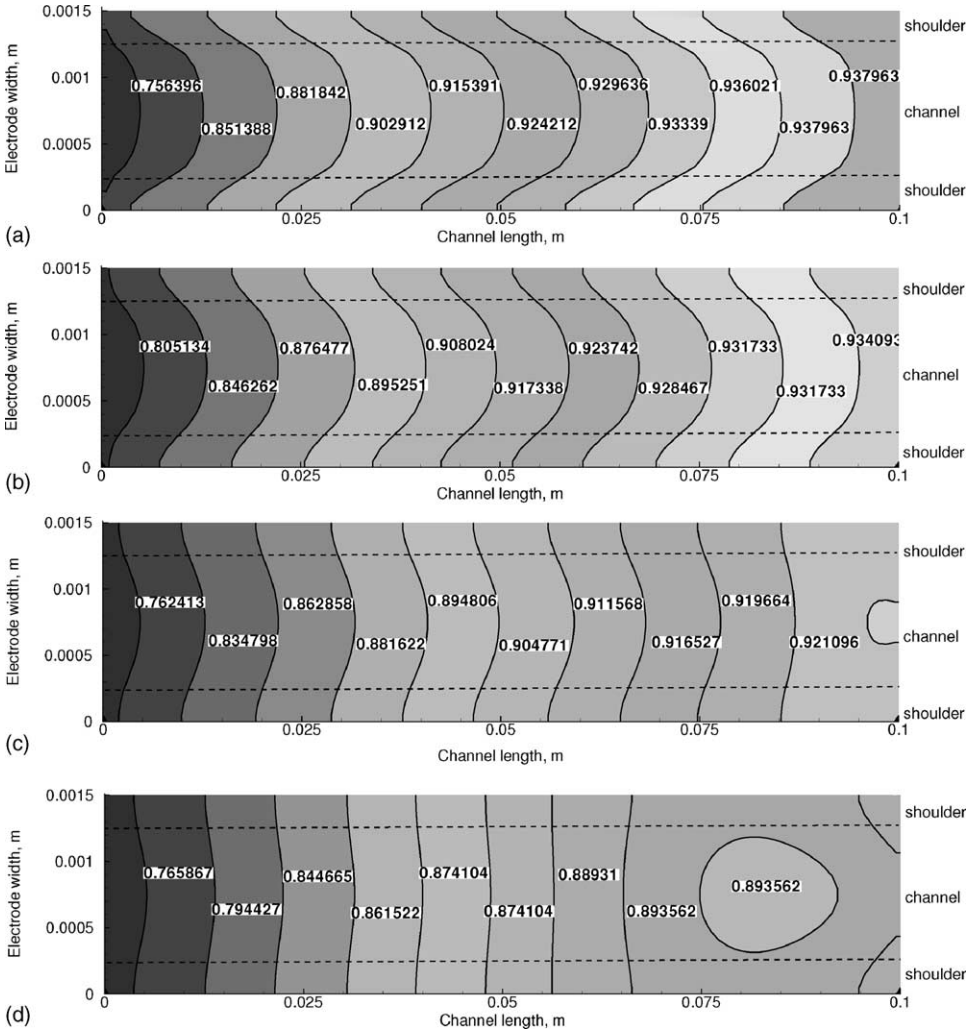

Fig. 17. Hydrogen distribution at the anode electrode/membrane interface at different electrode thicknesses of: (a) 1.0×10^{-4} m; (b) 2.0×10^{-4} m; (c) 4.0×10^{-4} m; (d) 6.0×10^{-4} m.

not reach the catalyst layer in an amount required for efficient electrochemical reaction to take place, as can be seen in Fig. 17.

Fig. 18(a and b) show the polarization and power density curves for the cell with different electrode thicknesses respectively. Increasing the electrode thickness from 1.0×10^{-4} m to 2.0×10^{-4} m results in better performance (average current density increases from 1.17×10^4 A m^{-2} to 1.2×10^4 A m^{-2}). Improvement is seen on further increasing the thickness to 4.0×10^{-4} m (average current density = 1.22×10^4 A m^{-2}). Mass transport limitation is seen to take place when a thickness of 6.0×10^{-4} m is used, where the polarization curve drops below the level in which a thinner electrode thickness was used. In general, a thinner electrode thickness is preferable as it improves the fluxes of reactant gases to the catalyst layer. The problem of dehydration at the anode can be easily reduced by sufficiently humidifying the inlet fuel so that the membrane can be kept hydrated to prevent drying. In this case, an electrode thickness of between 2.0×10^{-4} m to 4.0×10^{-4} m is preferable.

5.2. Parametric variations relevant to operating conditions

Apart from geometrical considerations, different operating conditions will also affect the performance of the fuel cell. Factors such as electrode permeability, operation using air or oxygen, among others, are believed to play a part. The role of all these factors can easily be studied using the current model. In this section, an analysis of such parameters has been carried out.

5.2.1. Effect of electrode permeability

Three different values of permeability are considered here: 1.0×10^{-8} m^2, 1.0×10^{-9} m^2 and 1.0×10^{-10} m^2. The role of the degree of permeability only affects the flux of species towards the catalyst layer by convection, due to the Darcy term. As the permeability value decreases, there is more resistance to the flow of species to the catalyst layer. This can be seen in Fig. 19. Decreasing the electrode permeability allows the reactant species to spread over to the shoulder area.

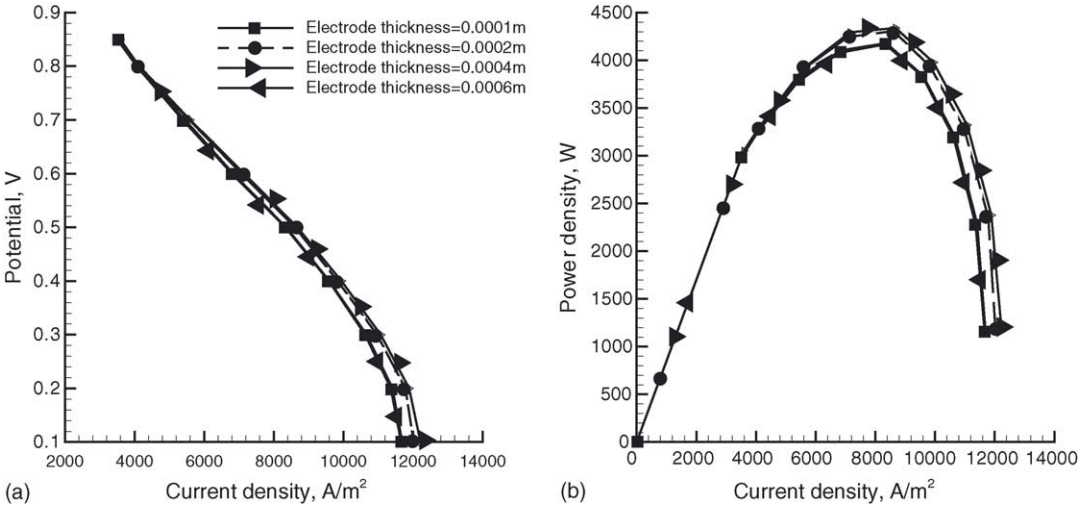

Fig. 18. (a) Polarization curve; (b) power density curve for the various electrode thicknesses.

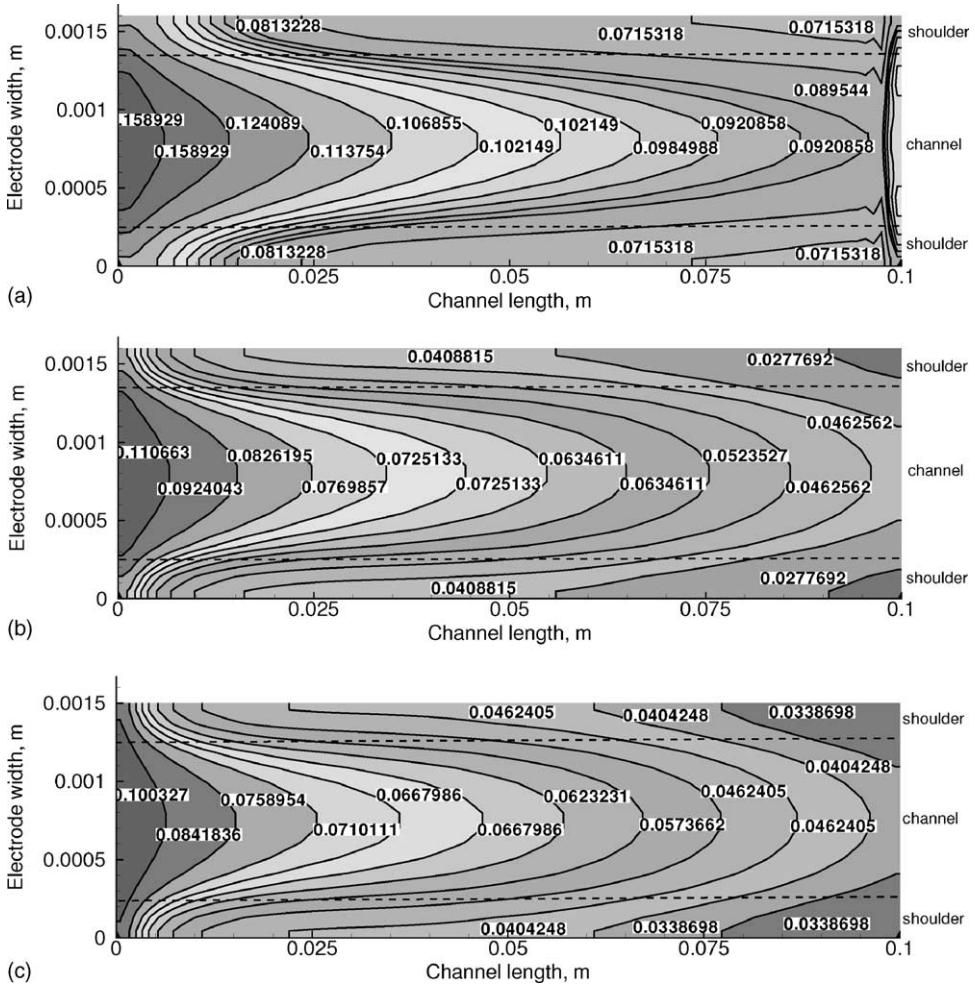

Fig. 19. Mass fraction of oxygen at the electrode/membrane interface for a permeability value of: (a) 1.0×10^{-8} m^2; (b) 1.0×10^{-9} m^2; (c) 1.0×10^{-10} m^2.

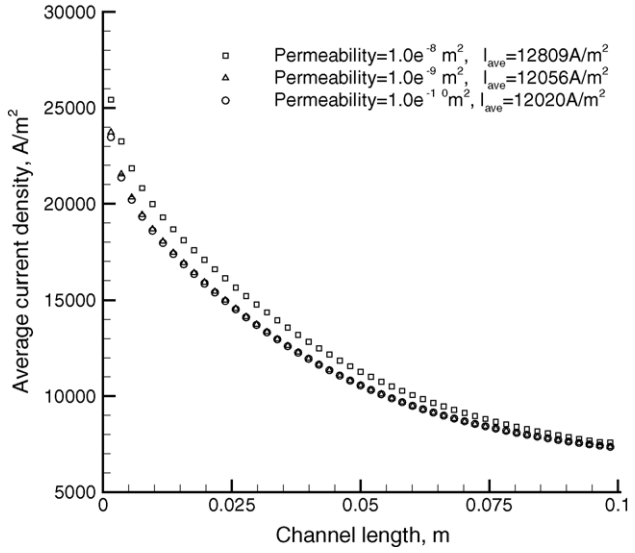

Fig. 20. Average current density at the electrode/membrane interface for the different permeability values.

This can enhance the gases to flow in the spanwise direction to better utilise the catalyst layer above the shoulder areas. However, this will only improve the cell performance if the shoulder area is greater than the channel area. As mentioned above, the use of a gas channel having a smaller width compare to the shoulder is not preferable. The abrupt changes that can be discerned in Fig. 19(a) close to the outlet originate from the very high absolute permeability (1.0×10^{-8} m^2) in the porous backing, leading to a higher convective flow in the streamwise and spanwise directions than for the two cases with lower permeability. Furthermore, the use of the outlet boundary condition here requires the flow to be fully developed, which is not the case here for such a high value of permeability. However, since the error is small, it is admissible to retain this boundary condition as the abrupt changes are only visible for the high permeability case.

The corresponding average current density for the three cases is given in Fig. 20. It can be seen that between the permeability value of 1.0×10^{-8} A m^{-2} to 1.0×10^{-9} A m^{-2}, a drop in average current density is obtained (1.28×10^4 A m^{-2} to 1.205×10^4 A m^{-2}). As the permeability value decreases further, no significant decrease in average current density is observed (1.202×10^4 A m^{-2}). Hence, there is a "limiting" permeability value whereby further reduction will not affect the overall performance of the fuel cell. This is further emphasised in the polarization and power density curves in Fig. 21(a and b) respectively. In general, it may be suggested that in terms of electrode properties, the porosity term may be more important in affecting the performance of a fuel cell. This means that diffusion plays a more important role than convection to transport the specie fluxes to the catalyst layer. From this study, it can be seen that lowering the permeability of the electrode beyond a value of 1.0×10^{-9} m^2 will not affect the performance of the cell.

5.2.2. *Effect of oxidant concentration*

In fuel cell operations, it is common to use air as the oxidant as air is readily available and does not need to be processed. However, the concentration of oxygen in air, which is the main reactant gas, is low. Performance will be affected unless a sufficiently high pressure is applied at the cathode inlet to increase the concentration of oxygen reaching the catalyst layer. This is because the current density is dependent on the partial pressure of oxygen. Fig. 22 compares the performance of the cell by using different concentrations of oxygen as the oxidant. The three cases considered are: air; air enriched with 30% of oxygen; pure oxygen.

It can be seen that not much difference is observed between all the three cases at high potential since low current density is produced and the need for efficient distribution of oxygen to the catalyst layer has not set in. At low potential, mass transport limitation begins to set in for the case where pure air is used (≈0.7 V). This is due to insufficient oxygen

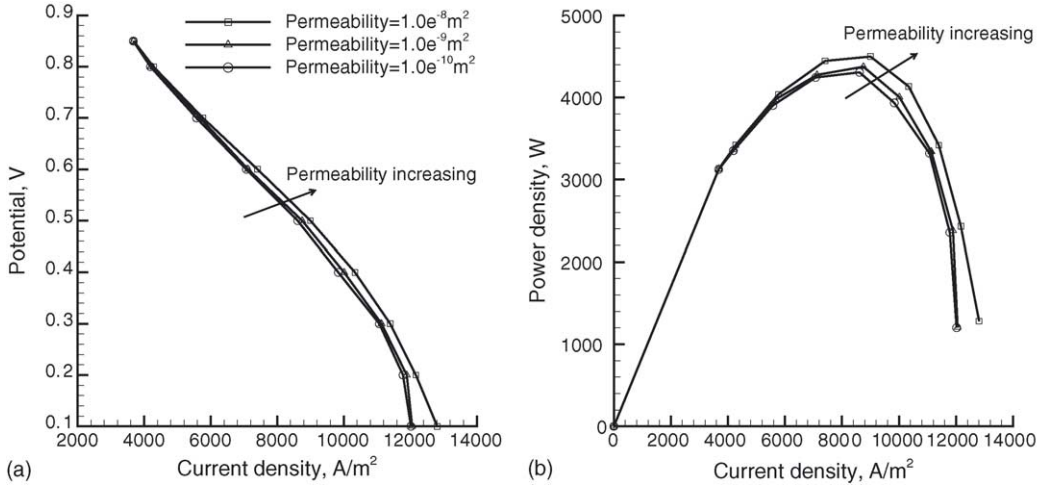

Fig. 21. (a) Polarization curve (b) power density curve for the various permeability cases.

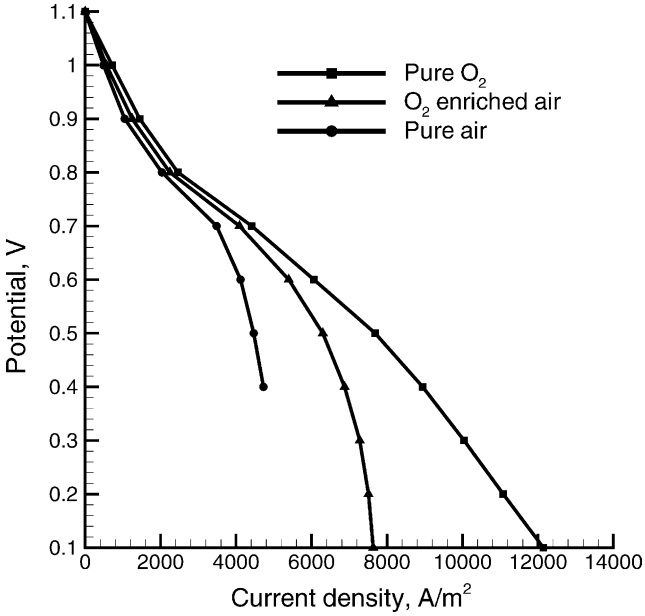

Fig. 22. Polarization curves for the different concentration of oxygen applied.

reaching the catalyst layer where electrochemical reaction takes place. With oxygen-enriched air, mass transport limitation takes place at a lower potential (≈ 0.6 V) and hence higher current density is possible. When pure oxygen is used as the oxidant, the polarization curve obtained is even higher since at the same applied pressure, a higher concentration of oxygen reaches the catalyst layer. No mass transport limitation is observed for the case with pure oxygen as the oxidant. The factor that prevents the cell from producing higher current when pure oxygen is used is probably due to the ohmic losses that occur at the membrane. Hence, the use of pure oxygen for fuel cell application is preferable although it has to be weighed against the added cost in doing so.

6. Conclusions

A three-dimensional model of a complete polymer electrolyte membrane fuel cell was implemented in an in-house code, which has been validated on a global basis with the work of Shimpalee et al. [22]. From the results obtained, the presence of liquid water on the cathode side is seen to lead to blockage of the electrode, causing mass transport limitation to the catalyst layer for electrochemical reaction to take place. This will result in a lower current density obtained.

The model was then validated on a local basis with experimental data of current density, which were obtained locally along the channel length. This is a stronger validation as it verifies current density obtained point by point along the channel length. Excellent agreement has been obtained between experimental data and the simulated results locally.

The net transport of water across the membrane from the anode to the cathode side was seen to decrease down the channel length. This is because the reactant concentration decreases down the channel, hence the current density obtained will be lower, leading to lower water produced on the cathode. This will reduce the effect of back diffusion, leading to a lower concentration of water on the anode side to be dragged by the protons across the membrane. Overall transport of water is seen to take place from the anode to the cathode. As a result, it is crucial to humidify the anode reactants to keep the membrane well hydrated to prevent dehydration.

Parameter variations relevant to the design of fuel cells have been carried out to study their effect on the cell operation. It has been found that a thinner electrode layer, and a smaller shoulder to channel width, is preferable since reactant gases are able to reach the catalyst layer with less resistance. Lowering the permeability of the electrode enhances species transport in the spanwise direction but this is only useful if the shoulder area is large, which is not preferred as in doing so prevents the reactant gases from being efficiently transported to the catalyst layer. Finally, introducing pure oxygen as the oxidant produces much higher current density (at the onset of mass transport limitation) compared to when pure air or air enriched with oxygen is used as the oxidant.

In general, there are many factors affecting the performance of the fuel cell simultaneously and all these factors have to be weighed comparatively together, depending on the kind of output desired for a particular application. It has been demonstrated in this work that it is relatively easy and straightforward to use the current CFD model when designing fuel cells to test various parameters to obtain the optimum operating conditions and cell geometry. A plot of the power density curve will show the condition under which maximum performance occurs. This will aid in designing and optimising fuel cell performance without the need to carry out expensive and time-consuming experiments.

Acknowledgements

The author gratefully acknowledges the financial support for this project by British Gas Asia Pacific and Loughborough University.

Appendix A

Boundary conditions

The boundary conditions are denoted with roman numerals for easy identification in the two geometries considered here, as shown in Figs. 2 and 5.

A.1. Inlet (I)

At the channel inlet, the known inlet velocity vectors and species mass fractions are specified. An “in” superscript represents condition at the inlet of the channel and the subscript

"i" refers to the individual species,

$$\boldsymbol{u} = \boldsymbol{u}^{\text{in}},\ m_i = m_i^{\text{in}}$$

A.2. Outlet (II)

At the channel outlet, zero gradient is applied to the velocity vectors and species mass fractions,

$$\frac{\partial \boldsymbol{u}}{\partial z} = \boldsymbol{0},\ \frac{\partial m_i}{\partial z} = 0$$

A.3. Wall (III)

For a porous media with an impermeable surface, the velocity normal to the surface is zero while the velocities in the other directions have a "slip" condition whereby their gradient is zero. Considering such a circumstance for the porous electrodes: In the *X–Z* plane,

$$\langle v \rangle = \frac{\partial \langle u \rangle}{\partial y} = \frac{\partial \langle w \rangle}{\partial y} = \frac{\partial m_i}{\partial y} = 0$$

In the *X–Y* plane,

$$\langle w \rangle = \frac{\partial \langle u \rangle}{\partial z} = \frac{\partial \langle v \rangle}{\partial z} = \frac{\partial m_i}{\partial z} = 0$$

For the non-porous impermeable surfaces, considering boundaries in the *X–Z* plane,

$$\boldsymbol{u} = \boldsymbol{0},\ \frac{\partial m_i}{\partial y} = 0$$

In the *X–Y* plane,

$$\boldsymbol{u} = \boldsymbol{0},\ \frac{\partial m_i}{\partial x} = 0$$

A.4. Symmetry (IV)

Assuming that end effects are negligible and that only a repeating unit of the complete cell needs to be modeled, each repeating unit will be bounded by two symmetry planes. For the porous electrodes, symmetries occur in the *Y–Z* plane,

$$\frac{\partial \langle \boldsymbol{u} \rangle}{\partial x} = \boldsymbol{0},\ \frac{\partial m_i}{\partial x} = 0$$

For the non-porous channels,

$$\frac{\partial \boldsymbol{u}}{\partial x} = \boldsymbol{0},\ \frac{\partial m_i}{\partial x} = 0$$

A.5. Porous/non-porous interface (V)

For complex geometries, different blocks have to be placed together. At the interface between the porous backing and the flow channels, the point wise velocities and pressure in the plain fluid (flow channels) must be coupled with their superficial counterparts in the porous medium. The mass fractions and fluxes of oxygen and water are continuous across the interface,

$$\boldsymbol{u}^{\text{np}} = \langle \boldsymbol{u} \rangle^{\text{p}},\ p^{\text{np}} = p^{\text{p}},\ -D\frac{\partial m_i^{\text{np}}}{\partial y} = -\in^{3/2} D\frac{\partial m_i^{\text{p}}}{\partial y},\ \mu\frac{\partial u}{\partial y} = \frac{\mu}{\in}\frac{\partial \langle u \rangle^{\text{p}}}{\partial y}$$

where the superscript "np" refers to properties in the non-porous region while p refers to properties in the porous region.

A.6. Membrane/catalyst interface (VI)

The electrochemistry at the membrane/catalyst interfaces on the cathode and anode side is implemented via source terms for the computational nodes adjacent to the membrane, as given in Table 1.

References

[1] D.M. Bernardi, Water balance calculations for solid polymer electrolyte fuel cells, J. Electrochem. Soc. 137 (11) (1990) 3344–3350.
[2] D.M. Bernardi, M.W. Verbrugge, A mathematical model of the solid polymer electrolyte fuel cell, J. Electrochem. Soc. 139 (9) (1992) 2477–2491.
[3] T.E. Springer, T.A. Zawodzinski, S. Gottesfeld, Polymer electrolyte fuel cell model, J. Electrochem. Soc. 138 (8) (1991) 2334–2342.
[4] M. Eikerling, Yu.I. Kharkats, A.A. Kornyshev, Yu.M. Volkovich, Phenomenological theory of electro-osmotic effect and water management in polymer electrolyte proton conducting membranes, J. Electrochem. Soc. 145 (8) (1998) 2684–2699.
[5] M. Wöhr, K. Bolwin, W. Schnurnberger, M. Fischer, W. Neubrand, G. Eigenberger, Dynamic modelling and simulation of polymer membrane fuel cell including mass transport limitation, Int. J. Hydrogen Energy 23 (3) (1998) 213–218.
[6] J.J. Baschuk, X. Li, Modelling of polymer electrolyte membrane fuel cells with variable degrees of water flooding, J. Power Sources 86 (2000) 181–196.
[7] A. Rowe, X. Li, Mathematical modelling of proton exchange membrane fuel cells, J. Power Sources 102 (2001) 82–96.
[8] G. Maggio, V. Recupero, L. Pino, Modelling polymer electrolyte fuel cells: an innovative approach, J. Power Sources 101 (2001) 275–286.
[9] T. Nguyen, R. White, A water and heat management model for proton exchange membrane fuel cells, J. Electrochem. Soc. 140 (1993) 2178–2186.
[10] J. Yi, T. Nguyen, Multicomponent transport in porous electrodes of proton exchange membrane fuel cells using the interdigitated gas distributors, J. Electrochem. Soc. 146 (1999) 38–45.
[11] H.P.L.H. van Bussel, F.G.H. Koene, R.K.A.M. Mallant, Dynamic model of solid polymer fuel cell water management, J. Power Sources 71 (1998) 218–222.
[12] K. Scott, S. Kraemer, K. Sundmacher, Gas and liquid mass transport in solid polymer electrolyte fuel cells, ICHEME Symposium Series No. 145, 1999, pp. 11–20.
[13] G. Squadrito, G. Maggio, E. Passalacqua, F. Lufrano, A. Patti, An empirical equation for polymer electrolyte fuel cell (PEFC) behaviour, J. Appl. Electrochem. 29 (1999) 1449–1455.
[14] V. Gurau, H. Liu, S. Kakac, Two-dimensional model for proton exchange membrane fuel cells, AIChE J. 44 (11) (1998) 2410–2422.
[15] J.S. Yi, T.V. Nguyen, An along the channel model for proton exchange membrane fuel cells, J. Electrochem. Soc. 145 (4) (1998) 1149–1159.

[16] D. Singh, D.M. Lu, N. Djilali, A two dimensional analysis of mass transport in proton exchange membrane fuel cells, Int. J. Eng. Sci. 37 (1999) 431–452.
[17] K. Dannenberg, P. Ekdunge, G. Lindbergh, Mathematical model of the PEMFC, J. Appl. Electrochem. 30 (2000) 1377–1387.
[18] I.M. Hsing, P. Futerko, Two-dimensional simulation of water transport in polymer electrolyte fuel cells, Chem. Eng. Sci. 55 (2000) 4209–4218.
[19] S. Um, C.Y. Wang, K.S. Chen, Computational fluid dynamics modelling of proton exchange membrane fuel cells, J. Electrochem. Soc. 147 (12) (2000) 4485–4493.
[20] P. Costamagna, Transport phenomena in polymeric membrane fuel cells, Chem. Eng. Sci. 56 (2001) 323–332.
[21] N.P. Siegel, M.W. Ellis, D.J. Nelson, M.R. von Spakovsky, A two dimensional computational model of a PEMFC with liquid water transport, J. Power Sources 128 (2) (2004) 173–184.
[22] S. Shimpalee, S. Dutta, W.K. Lee, J.W. Van Zee, Effect of humidity on PEM fuel cell performance part II-numerical simulation, Proc. ASME Heat Transfer Div. 364-1 (1999) 367–374.
[23] H.N. Neshat, S. Shimpalee, S. Dutta, W.K. Lee, J.W.V. Zee, Predicting the effect of gas flow channel spacing on current density in PEM fuel cells, in: Proceedings of the ASME Advanced Energy Systems Division, AES-Vol. 39, 1999, pp. 337–350.
[24] S. Dutta, S. Shimpalee, J.W. Van Zee, Three dimensional numerical simulation of straight channel PEM fuel cells, J. Appl. Electrochem. (1999) 135–146.
[25] S. Dutta, S. Shimpalee, J.W. Van Zee, Numerical prediction of mass exchange between cathode and anode channels in a PEM fuel cell, Int. J. Heat Mass Transfer 44 (2001) 2029–2042.
[26] T. Berning, N. Djilali, Three dimensional computational analysis of transport phenomena in a PEM fuel cell, in: Proceedings of the Seventh Groove Symposium, London, 2001.
[27] T. Berning, N. Djilali, Three dimensional numerical analysis of fluid flow, heat and mass transfer in fuel cells, J. Power Sources 106 (2002) 284–294.
[28] T. Berning, N. Djilali, Three dimensional computational analysis of transport phenomena in a PEM fuel cell—a parametric study, J. Power Sources 124 (2) (2003) 440–452.
[29] T. Zhou, H. Liu, A general three-dimensional model for proton exchange membrane fuel cells, Int. J. Transport Phenomena 3 (2001) 177–198.
[30] T.C. Jen, T. Yan, S.H. Chan, Chemical reacting transport phenomena in a PEM fuel cell, Int. J. Heat Mass Transfer 46 (22) (2003) 4157–4168.
[31] S. Um, C.Y. Wang, Three dimensional analysis of transport and electrochemical reactions in polymer electrolyte fuel cells, J. Power Sources 125 (1) (2004) 40–51.
[32] P.T. Nguyen, T. Berning, N. Djilali, Computational model of a PEM fuel cell with serpentine gas flow channels, J. Power Sources 130 (1-2) (2004) 149–157.
[33] S.M. Senn, D. Poulikakos, Three dimensional computational modeling of polymer electrolyte fuel cells, in: Proceedings Fuel Cell Research Symposium-Modeling and Experimental Validation, 2004.
[34] T.E. Springer, T.A. Zawodzinski, S. Gottesfeld, Modelling of batteries and fuel cells, in: R.E. White, M.W. Verbrugge, J.F. Stockel (Eds.), The Electrochemistry Society Softbound Proceedings Series, Pennington, NJ, 1991, p. 209, PV91-10.
[35] K.W. Lum, Three-dimensional computational modelling of a polymer electrolyte membrane fuel cell, Thesis submitted in partial fulfilment for the award of Degree of Doctor of Philosophy of Loughborough University, 2003.
[36] M.J. Potter, Parametric analysis of a solid polymer fuel cell using current distribution mapping, PhD thesis, Loughborough University, 1999.
[37] J.C. Slattery, R.B. Bird, AIChE J. 4 (1958) 137–142.
[38] D.A.G. Bruggeman, Ann. Phys. (Leipzig) 24 (1935) 636.
[39] S.V. Patankar, Numerical Heat Transfer and Fluid Flow, Hemisphere, New York, 1980.
[40] C.M. Rhie, W.L. Chow, Numerical study of the turbulent flow past an airfoil with trailing edge separation, AIAA J. 21 (11) (1983) 1525–1532.
[41] Z.H. Wang, C.Y. Wang, K.S. Chen, Two-phase flow and transport in the air cathode of proton exchange membrane fuel cells, J. Power Sources 94 (2001) 40–50.
[42] L. You, H. Liu, A two-phase flow and transport model for the cathode of PEM fuel cells, Int. J. Heat Mass Transfer 45 (2002) 2277–2287.
[43] S. Mazumder, J.V. Cole, Rigorous 3-D mathematical modeling of PEM fuel cells II: model predictions with liquid water transport, J. Electrochem. Soc. 150 (11) (2003) A1510–A1517.
[44] T. Berning, N. Djilali, A 3D, multiphase, multicomponent model of the cathode and anode of a PEM fuel cell, J. Electrochem. Soc. 150 (12) (2003) A1589–A1598.
[45] J. Ihonen, M. Mikkola, G. Lindbergh, Flooding of gas diffusion backing in PEFCs, physical and electrochemical characterization, J. Electrochem. Soc. 151 (2004) 1152–1161.